



**HAL**  
open science

# Investigation techniques and physical aspects of the angle of repose of granular matter

Sacha Duverger, Vasileios Angelidakis, Sadegh Nadimi, Stefano Utili, Stéphane Bonelli, Pierre Philippe, Jérôme Duriez

## ► To cite this version:

Sacha Duverger, Vasileios Angelidakis, Sadegh Nadimi, Stefano Utili, Stéphane Bonelli, et al.. Investigation techniques and physical aspects of the angle of repose of granular matter. *Granular Matter*, 2024, 26 (1), pp.20. <10.1007/s10035-023-01378-z>. <hal-04222127>

**HAL Id: hal-04222127**

**<https://hal.inrae.fr/hal-04222127v1>**

Submitted on 28 Sep 2023

**HAL** is a multi-disciplinary open access archive for the deposit and dissemination of scientific research documents, whether they are published or not. The documents may come from teaching and research institutions in France or abroad, or from public or private research centers.

L'archive ouverte pluridisciplinaire **HAL**, est destinée au dépôt et à la diffusion de documents scientifiques de niveau recherche, publiés ou non, émanant des établissements d'enseignement et de recherche français ou étrangers, des laboratoires publics ou privés.



HAL Authorization

# Investigation techniques and physical aspects of the angle of repose of granular matter

Sacha Duverger<sup>1</sup>, Vasileios Angelidakis<sup>2,3</sup>, Sadegh Nadimi<sup>2</sup>, Stefano Utili<sup>2</sup>, Stéphane Bonelli<sup>1</sup>, Pierre Philippe<sup>1</sup> and Jérôme Duriez<sup>1\*</sup>

<sup>1</sup>INRAE, Aix Marseille Univ, RECOVER, Aix-en-Provence, France.

<sup>2</sup>School of Engineering, Newcastle University, Newcastle upon Tyne, United Kingdom.

<sup>3</sup>Institute for Multiscale Simulation, Friedrich-Alexander-Universität Erlangen-Nürnberg, Germany.

\*Corresponding author(s). E-mail(s): [jerome.duriez@inrae.fr](mailto:jerome.duriez@inrae.fr);

Contributing authors: [sacha.duverger@inrae.fr](mailto:sacha.duverger@inrae.fr); [vasileios.angelidakis@fau.de](mailto:vasileios.angelidakis@fau.de);  
[sadegh.nadimi-shahraki@newcastle.ac.uk](mailto:sadegh.nadimi-shahraki@newcastle.ac.uk); [stefano.utili@newcastle.ac.uk](mailto:stefano.utili@newcastle.ac.uk);  
[stephane.bonelli@inrae.fr](mailto:stephane.bonelli@inrae.fr); [pierre.philippe@inrae.fr](mailto:pierre.philippe@inrae.fr);

## Abstract

The repose of granular materials is investigated via two different Discrete Element Method (DEM) implementations in comparison with an experimental reference from a recently proposed benchmark setup. On a methodological standpoint, a rigorous measurement method of the angle of repose (AOR) is first proposed for plane-strain and axisymmetric conditions as encountered in the reference experiments. Additionally, two systematic procedures are designed in order to also determine the void ratio of the heap, as a fundamental property of granular matter possibly influencing the AOR. A physical discussion is then developed on the role of particle shape, considering the non-spherical nature of reference particles with a convexity value of  $C = 0.954$ . Adopting non-convex multi-spheres aggregates (i.e. clumps), the first DEM modelling approach successfully predicts the AOR within a 8% tolerance. After a convex simplification that neglects local concavities, another approach based on potential particles underestimates to a greater extent the AOR, bringing it down from  $35.95 \pm 0.88^\circ$  to  $31.26 \pm 0.95^\circ$ . For the loading setup(s) at hand, the AOR is eventually shown to bear no constitutive nature. It is for instance independent of initial void ratio but is still different than the critical friction angle. The latter may actually serve as a lower bound for the process-dependent AOR. These conclusions are drawn from a statistical analysis of a large set of results, accounting for the random nature of the microscopic arrangement in the studied process.

**Keywords:** Angle of repose; Discrete Element Method; Non-spherical particles

# 1 Introduction

Under loading, particulate matter strains in the form of a fluid-like flow as long as the applied load is high enough. Then, once loading no longer prevails against internal dissipation in terms of energy input, particulate matter comes at rest in a solid-like heap configuration, especially in the absence of cohesion or adhesion. The corresponding slope, expressed in terms of an angle of repose (AOR), rules the spatial extents of the deposit for a given matter quantity. The AOR is therefore of interest for countless applications involving particulate materials, for instance the design of industrial facilities for granular-conveying processes, or the prediction of the coverage of natural deposits after e.g. snow or rock avalanches. Several standardised measurement procedures have been proposed in the literature to measure the AOR of granular materials employing empirical and geometrical concepts [1, 2] but they unfortunately often lead to inconsistent results, as demonstrated in [3], and new measurement devices are still being proposed [4]. As such, an one-to-one correlation of the AOR to theoretically-established mechanical properties is not always demonstrated even though the AOR may be often considered as a material property, e.g. in [5] in geotechnics or in [6, 7] for the purpose of DEM calibration. A part of the complexity certainly stems from an influence of non-constitutive parameters such as the heap construction history

[8] and possible geometrical effects [9, 10]. The latter comes in addition to the more natural influence of physical microscopic properties such as particle shape [11, 12] and contact friction [11, 9, 12], as well as mesoscopic ones, such as fabric [12]. Last, it should be noted that granular heaps may not systematically conform to a linear slope [13, 14] which may prevent one to define a single-valued AOR.

Following up on these previous works, the aim of the present manuscript is twofold. First, rigorous simulation and measurement methods are proposed in order to ease evergoing AOR studies. Second, with the help of these methods, an in-depth study is conducted in order to gain further insights on the AOR variations with respect to physical parameters. The present analysis combines the use of two Discrete Element Method (DEM) approaches and existing experimental results recently proposed by the Japanese Geotechnical Society (JGS) as part of a round robin series of tests [4, 15].

The remainder of the article is as follows. Section 2 first recalls the JGS reference experiments [4] and the two DEM formulations which are both executed within the YADE code [16] but differ in the way the exact shape of the grains is described. Section 3 then introduces new methods enhancing AOR studies, namely a systematic definition of the AOR value after detection of the

61 external slope and versatile measurement meth-  
 62 ods of the packing compacity (void ratio) of the  
 63 heap since the latter is a fundamental property  
 64 of granular matter. It also provides a discus-  
 65 sion on computational aspects of the two DEM  
 66 approaches used to simulate the same JGS exper-  
 67 iments. Section 4 finally provides new insights on  
 68 the role of some physical parameters on the AOR  
 69 value, after conducting a large number of DEM  
 70 simulations interpreted in a statistics fashion for  
 71 the sake of robust conclusions.

## 72 2 Reference benchmark 73 experiments and DEM 74 formulations

### 75 2.1 Reference benchmark 76 experiments

77 Measurements of AOR data have been recently  
 78 proposed by the JGS as part of a round robin test  
 79 organised within the activities of Technical Com-  
 80 mittee 105 (TC105: Geo-Mechanics from Micro  
 81 to Macro) of the International Society for Soil  
 82 Mechanics and Geotechnical Engineering (ISS-  
 83 MGE) [4] and will serve here as reference. In  
 84 a first step, data only included an experimen-  
 85 tal characterization of the granular material at  
 86 hand, together with properties of the two experi-  
 87 mental setups used for AOR measurement, before  
 88 that blind DEM predictions of the AOR values

89 could be proposed by international participants to  
 90 the round robin and compared with experimental  
 91 values [15].

92 An artificial granular material was considered  
 93 with non-spherical particles made of 3D-printing  
 94 resin. Particles constituting the mono-dispersed  
 95 material resemble a tetrahedral arrangement of  
 96 four spheres clumped together (see Figure 1). Indi-  
 97 vidual spheres have a radius of  $r_s = 0.3101\text{ cm}$ ,  
 98 while each global particle is inscribed in a radius  
 99  $r_{clump} = 0.5\text{ cm}$ .

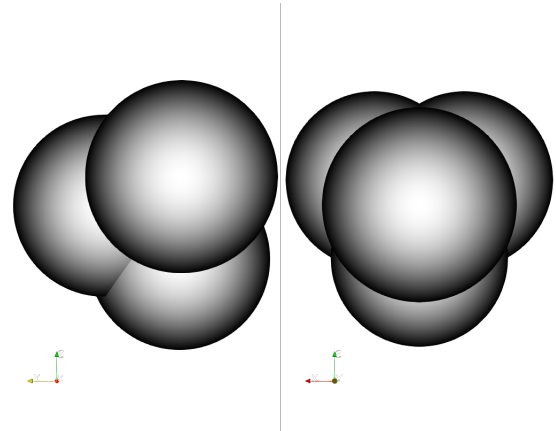


**Fig. 1:** Physical particle made of 4 clumped spheres.

100 The considered AOR setups consist of two  
 101 devices in the form of either a cylindrical (see  
 102 Figure 2) or cuboidal (see Figure 3) container with  
 103 acrylic walls, aiming to compare how the AOR  
 104 varies for heaps of different geometries. For the  
 105 cylindrical case forming an axisymmetric configu-  
 106 ration, the container encloses the particles before  
 107 the surrounding wall is lowered until a small,

108 final, height of 1 cm. For the second device cor-  
 109 responding to a plane-strain configuration of the  
 110 repose state, the cuboidal box encloses the parti-  
 111 cles initially, until one of the side walls is removed  
 112 upwards, leaving eventually only a fixed 0.5 cm  
 113 ridge to retain the lowest particles on that side.  
 114 The reference number of particles, walls' velocity  
 115 and boxes' dimensions are given in Table 1 for  
 116 both configurations, as per the specifications of  
 117 the round robin test. These parameters were also  
 118 set to different values for some series of simulations  
 119 in this study, see Section 4.5 for what concerns  
 120 the number of particles and boxes' dimensions or  
 121 Appendix C for the walls' velocity.

## 122 2.2 DEM shape description with 123 clump and potential particles 124 approaches

### 125 2.2.1 Clumps of spheres

126 In line with the physical particles at hand (see  
 127 Figure 1), a first DEM approach adopts the tra-  
 128 ditional multi-sphere technique to simulate non-  
 129 spherical particles. A rigid agglomeration of four  
 130 spheres is created to reflect the particle morphol-  
 131 ogy as a so-called clump, e.g. as shown in [17].  
 132 This technique leads to an increased total number  
 133 of discrete elements in a simulation, compared to  
 134 the number of physical particles, however it ben-  
 135 efits from the low computational cost of collision  
 136 detection among spheres. To define the inertial

137 properties of a clump, many DEM codes still  
 138 simply add the masses of the clump members  
 139 and directly combine their inertia matrices, which  
 140 leads to an overestimation in the case of clumps  
 141 with overlapping members, like the one adopted  
 142 to simulate the present 3D-printed particle. To  
 143 mitigate this issue, methods to adjust the den-  
 144 sity of each sphere-member have been proposed  
 145 in the literature, such as the one of Ferrellec and  
 146 McDowell [18] to correct mass and inertia at the  
 147 cost of some pre-processing efforts. YADE, along  
 148 with PFC, provide an alternative solution, where a  
 149 three-dimensional grid of voxels is generated in the  
 150 bounding box of the particle, and it is evaluated  
 151 for each voxel whether it belongs to at least one  
 152 sphere-member of the clump. For the particles at  
 153 hand in this study, a grid size of  $1000 \times 1000 \times 1000$   
 154 voxels is used to estimate the volume (and thus the  
 155 mass) and inertia tensor, with negligible discreti-  
 156 sation error induced by the grid resolution, since  
 157 finer grids led to the same inertial properties.

### 158 2.2.2 Potential particles

159 While the above clump approach is a straightfor-  
 160 ward DEM strategy for describing the physical  
 161 particles at hand (Figure 1), a comparison is car-  
 162 ried out with a second approach using the so-called  
 163 “potential particles” introduced by Houlsby [19],  
 164 and extended to three-dimensions by Boon et al.  
 165 [20]. The potential particles are generalised convex

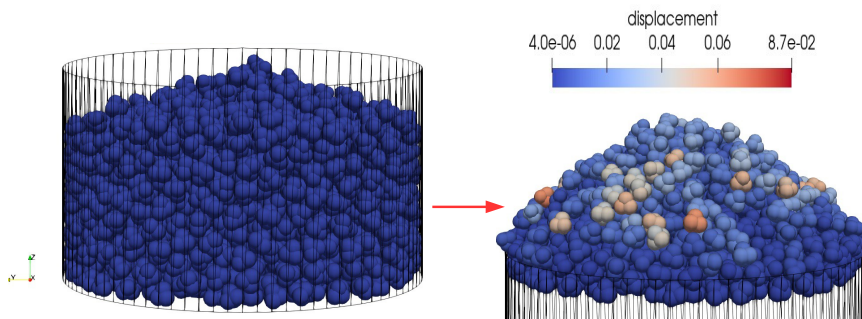


**Fig. 2:** Initial (left) and final (right) states of the heap in the axisymmetric configuration.

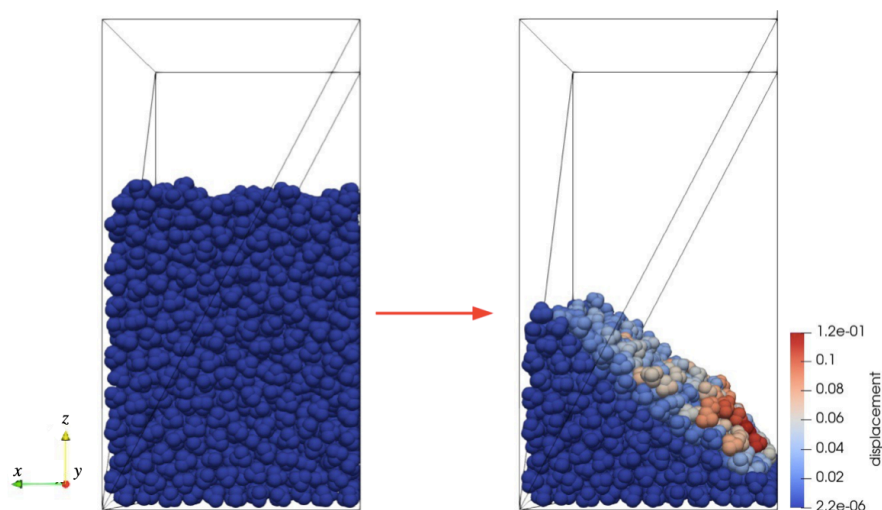


**Fig. 3:** Initial (left) and final (right) state of the heap in the plane strain configuration.

166 non-spherical particles, assembled as a combina-  
 167 tion of 2<sup>nd</sup> degree polynomial functions and a  
 168 fraction of a sphere, while their edges are rounded  
 169 with a user-defined radius. In line with their inher-  
 170 ent restriction to convexity, rather common in  
 171 DEM with complex shapes, e.g. as in [8], the  
 172 additional consideration of using potential parti-  
 173 cles will illustrate the mechanical implications of

neglecting the concavity of the physical particles  
 to the AOR.

For the exact definition of a potential particle,  
 as detailed in Boon et al. [20], a set of  $N$  planes  
 are assembled such that their normal vectors point  
 outwards, with their interior forming a convex  
 polytope. These planes are summed quadratically  
 and expanded by a distance  $r$ , which is also related  
 to the radius of the curvature at the corners.

**Table 1:** Default configuration of AOR simulations

Configuration	Initial number of particles	Side wall velocity	Container height	Container width
Axisymmetric	$N_{part} = 2,468$	$V_{cyl} = 6.67 \cdot 10^{-4} \text{ m/s}$	$H_{cyl} = 9 \cdot 10^{-2} \text{ m}$	$R_{cyl} = 8 \cdot 10^{-2} \text{ m}$
Plane strain	$N_{part} = 2,150$	$V_{par} = 4.3 \cdot 10^{-2} \text{ m/s}$	$H_{par} = 1.9 \cdot 10^{-1} \text{ m}$	$L_{par} = 1 \cdot 10^{-1} \text{ m}$

183 Furthermore, a 'shadow' spherical term is added,  
 184 where  $R$  is its radius and  $0 < k \leq 1$  denotes the  
 185 fraction of sphericity of the particle. A value of  
 186  $k \approx 0$  corresponds to a nearly sharp polyhedron,  
 187 while  $k = 1$  corresponds to a perfectly spherical  
 188 particle.

189 A potential particle is eventually defined by a  
 190 potential function  $f$  as in Equation 1:

$$f(x, y, z) = (1 - k) \left( \sum_{i=1}^N \frac{\langle a_i x + b_i y + c_i z - d_i \rangle^2}{r^2} - 1 \right) + k \left( \frac{x^2 + y^2 + z^2}{R^2} - 1 \right) \quad (1)$$

191 where  $(a_i, b_i, c_i)$  is the normal vector of the  $i^{th}$   
 192 plane in local particle coordinates,  $d_i$  is the dis-  
 193 tance of the plane to the local origin and  $\langle \rangle$  are  
 194 Macaulay brackets, i.e.,  $\langle x \rangle = x$  for  $x > 0$ ;  $\langle x \rangle = 0$   
 195 for  $x \leq 0$ .

196 This potential function takes zero values ( $f =$   
 197  $0$ ) on the particle surface, negative values ( $f < 0$ )  
 198 inside the particle and positive values ( $f > 0$ ) out-  
 199 side. In this sense, some similarity can be found  
 200 with the Level-Set Discrete Element Method (LS-  
 201 DEM) [21, 22, 23] where the potential is the actual  
 202 distance function, unlike here. The contact point  
 203 between two potential particles is found as the

optimal point of a Second Order Conic optimi-  
 sation Problem (SOCP) describing the contact  
 detection problem, representing a point nearest  
 to both the particles, based on their potential  
 functions.

Here, the mathematical formulation of the  
 potential particles enables one to approximate the  
 given particle shape by a rounded tetrahedron. To  
 decide which planes to use in order to assemble  
 the potential particle of the 3D-printed material,  
 two criteria were considered, a physical and a  
 practical one, with the latter aiming to achieve  
 post-processing convenience: (1) First, the poten-  
 tial particle should capture the morphology of the  
 physical particle as faithfully as possible in terms  
 of size, surface curvature, mass and inertia of the  
 given physical particle, or other shape descriptors  
 such as the sphericity; (2) To achieve comparable  
 results with the clump models, for the evaluation  
 of the AOR, it is convenient for each potential par-  
 ticle to be monitored via four points being located  
 at the same positions than the centers of the four  
 spheres making the tetrahedron. Thus, it is sought  
 that the potential particle has a straightforward  
 analogy to this format. To satisfy these criteria,

**Table 2:** Coefficients defining the planes making the faces of the tetrahedral potential particle as described in Equation 1.

Plane coefficient	Plane 1	Plane 2	Plane 3	Plane 4
a	0	$\sqrt{2/3}$	0	$-\sqrt{2/3}$
b	0	$\sqrt{2/3}$	$2\sqrt{2/3}$	$\sqrt{2/3}$
c	-1	1/3	1/3	1/3
d (cm)	0.063299	0.063299	0.063299	0.063299

the planes used to assemble the potential particle were chosen as the faces of the tetrahedron connecting the centers of the spheres making the physical particle (see Table 2). This approach can be generalised to approximate any convex shape, given a tessellation of its surface, or a multi-sphere representation of a particle made of spheres with equal radii.

To match the local surface curvature of the physical particle, a radius  $r = r_s$  was chosen in Equation 1 to control the roundness of the edges and corners of the potential particle consistently with the  $r_s$  radius of each individual sphere in the physical particle. The radius of the shadow particle was assigned to  $R = \sqrt{2}r_s$ , to capture the curvature of faces of the given particle shape. The remaining parameter needed to be calibrated in order to match the given particle shape was the parameter  $k$ , which controls the curvature of the faces. A value of  $k = 0.65$  led to a good match with the target geometry, i.e. it achieves an adequate representation of both the overall form of the real particle and features such as its main

dimensions, while also approximating its curvature. The parameters  $r$ ,  $R$  and  $k$  were chosen via a trial-and-error procedure. Figure 4 demonstrates visually the geometrical faithfulness of the generated potential particle to the shape of the real, physical particle.

In addition to modelling the rounded, tetrahedral-like particles, the potential particles also serve to simulate cuboidal elements of various sizes, making the moving and still parts of the plane-strain and axisymmetric devices, enabling one to build YADE models using a single, unified approach and contact detection algorithm.

### 2.2.3 Particle shape characterisation

As demonstrated in Figure 4, the selected potential particle can approximate the morphology of the physical particle faithfully, as it qualitatively represents the main dimensions of the particle, determining particle form, along with the curvatures of its edges/corners, relating to particle roundness. However, the potential particles modelling approach cannot represent the concavity of the physical particle. A quantitative characterisation of particle form was also performed using SHAPE [24], an open-source shape analysis software for three-dimensional particles, in order to quantify in Table 3 the similarity between the physical particle and its two numerical replicates. To this end, the surface mesh of the physical particle was first tessellated from its corresponding DEM

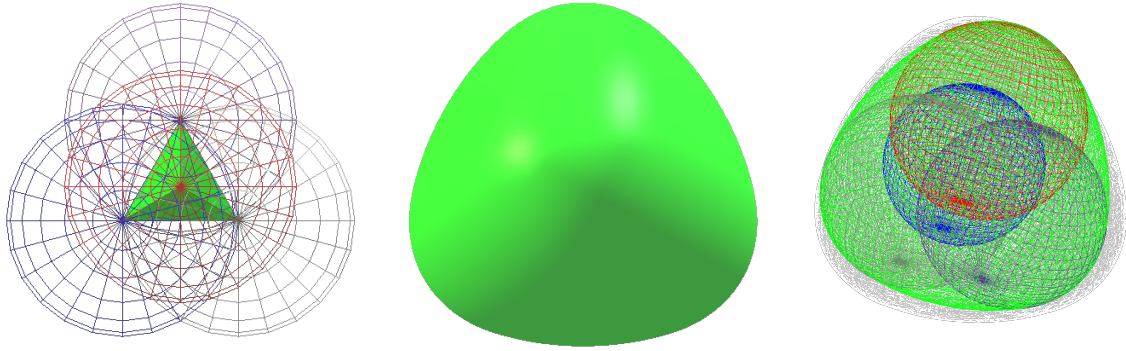


**Fig. 4:** Clumped tetrahedral particle (left); fitted potential particle (middle); overlap of the two (right).

282 clump, using the surface extraction module of  
 283 CLUMP [17], an open-source code for the generation  
 284 and processing of multi-sphere particles. Particle  
 285 shape was characterised in terms of volume, sur-  
 286 face area, principal inertia values, convexity and  
 287 true sphericity. Convexity is calculated in [0;1] as  
 288 the ratio of the volume of each particle divided by  
 289 the volume of its convex hull, while true sphericity,  
 290 also ranging in [0;1], is the ratio of the surface area  
 291 of a sphere with equal volume to the surface area  
 292 of the particle [25]. It becomes evident from Table  
 293 3 that both the physical and the potential particle  
 294 take high values of convexity and true sphericity  
 295 ( $>0.90$ ). It may furthermore be noted that both  
 296 the multi-sphere and the potential particle share  
 297 the same minimal bounding box and thus main  
 298 particle dimensions, resulting to the same flatness  
 299 and elongation values considering indices that rely  
 300 on these main particle dimensions. Therefore, flat-  
 301 ness and elongation were not monitored in this  
 302 study, as convexity and true sphericity were the

two differentiating factors between the two stud- 303  
 304 ied particle representations, from a morphological  
 305 standpoint. Table 3 also offers a comparison with  
 306 a so-called "non-uniform density" clump approach  
 307 that would count multiple times the overlapping  
 308 parts of the sphere-members in the calculation of  
 309 volume and inertia, which would correspond to  
 310 density showing a spatial increase at areas where  
 311 spheres overlap.

As expected, the considered potential parti- 312  
 313 cle has larger values of volume and geometric  
 314 inertia. The effect of the resulting increased parti-  
 315 cle mass is investigated in Section 4.1 by scaling  
 316 down their density so the potential particle has  
 317 the same mass as the real particle, i.e.  $\rho_{rescaled} =$   
 318  $\rho \times 3.3304 \times 10^{-7} / (3.9248 \times 10^{-7}) \approx 943 \text{ kg/m}^3$ .

Bringing the error on mass down to zero 319  
 320 through this scaling, the error in inertia values for  
 321 potential particles drops from 27.17 % down to  
 322 7.96 %. It is interesting to note that using over-  
 323 lapping spheres with no correction for uniform

**Table 3:** Shape parameters of the physical particle in comparison with various DEM approaches

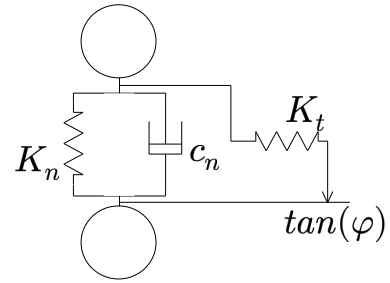
Shape characteristics	(1) Physical particle or present clump approach	(2) Potential Particle	$\frac{(2)-(1)}{(1)}$	(3) Clump approach with non-uniform density	$\frac{(3)-(1)}{(1)}$
Volume (m <sup>3</sup> )	$3.3304 \times 10^{-7}$	$3.9248 \times 10^{-7}$	17.85%	$4.9965 \times 10^{-7}$	50.03%
Surface area (m <sup>2</sup> )	$2.491 \times 10^{-4}$	$2.632 \times 10^{-4}$	5.66%	$2.491 \times 10^{-4}$	0
Inertia tensor/ $\rho$ (m <sup>5</sup> )	$\begin{bmatrix} 2.584 & 0 & 0 \\ 0 & 2.584 & 0 \\ 0 & 0 & 2.584 \end{bmatrix} \times 10^{-12}$	$\begin{bmatrix} 3.286 & 0 & 0 \\ 0 & 3.286 & 0 \\ 0 & 0 & 3.286 \end{bmatrix} \times 10^{-12}$	27.17%	$\begin{bmatrix} 3.123 & 0 & 0 \\ 0 & 3.123 & 0 \\ 0 & 0 & 3.123 \end{bmatrix} \times 10^{-12}$	20.86%
Convexity	0.954	1	4.82%	0.954	0
True sphericity	0.9328	0.9849	5.59%	0.9328	0

density i.e. inner overlaps would lead to an error of 50.03 % for the volume and 20.86 % for the eigenvalues of the principal inertia tensor.

### 2.3 DEM contact formulation

At each contact, kinematics is defined with the normal and tangential relative displacements of the particles,  $u_n$  and  $\underline{u}_t$  respectively. For the clump model, contacts are detected between spheres belonging to different clumps and  $u_n$  is computed as the norm of the branch vector to the spheres' radii, while  $\underline{u}_t$  is computed incrementally, see e.g. [23]. For the potential particle model,  $u_n$  is computed using a bracketed line-search algorithm as detailed in Boon et al. [20], deployed along the contact normal direction and starting from the contact point, to detect two points on the surface of each particle, forming a branch vector, the norm of which is considered as the sought approaching distance. The shear increment of  $\underline{u}_t$  is calculated in a similar manner as for spheres, i.e. via time integration of the shear component of the relative velocity during contact.

The same contact model applies to these kinematic quantities for both the clump and the potential particle approaches, accounting for linear visco-elasticity and friction (Figure 5). In the

**Fig. 5:** Contact model with visco-elasticity and friction.

normal direction, a spring with a normal stiffness  $K_n$  is associated in parallel with a viscous damper of coefficient  $c_n$ , as formulated in Equation 2. In the tangential direction, a spring with a tangential stiffness  $K_t$  is associated in series with a frictional slider (contact friction angle  $\varphi$ ), see Equation 3.

$$F_n = \max(K_n u_n + c_n \dot{u}_n, 0) \quad (2)$$

$$|\underline{F}_t| = \min(K_t |\underline{u}_t|, F_n \tan(\varphi)) \quad (3)$$

One should note that different YADE classes implement the above Eqs. 2-3 for clumps and potential particles with different methods of expressing the viscous damping coefficient  $c_n$ . In all cases, a desired normal restitution coefficient  $e_n$  serves a starting point before some differences appear in the YADE workflow, as detailed in Appendix A. Nevertheless, Figure 6 illustrates the common dissipative behavior of both models with the same  $F_n(u_n)$  curves in the case of two colliding spheres (obtained after using  $k = 1$  in Equation 1 for the PP approach) with an initial relative normal velocity  $V$ , demonstrating the consistency of the two implementations of visco-elasticity.

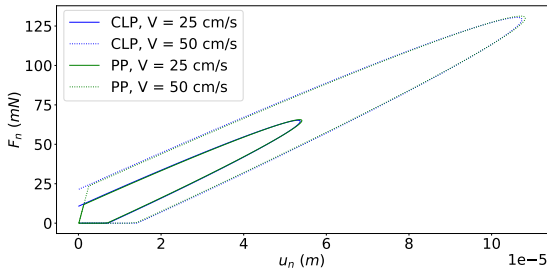
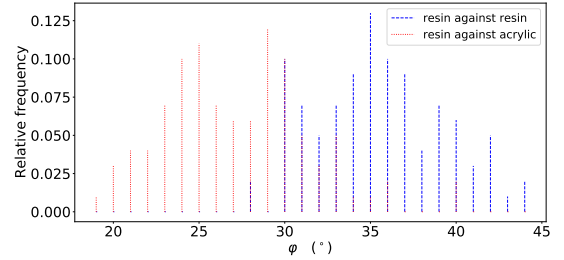


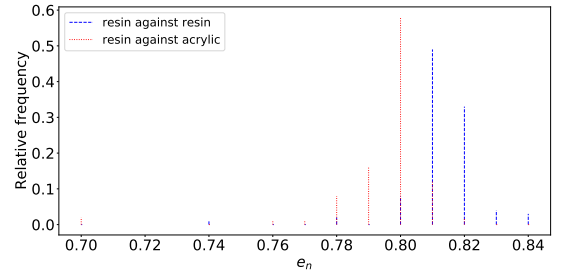
**Fig. 6:** Contact behaviour for different impact velocities in the two DEM approaches.

In the framework of the round robin test, the JGS measured the contact friction angle  $\varphi$  and the normal restitution coefficient  $e_n$  for resin against acrylic contacts and for resin against resin contacts, as well as the normal stiffness  $K_n$  for resin spheres. Experimental measurements exhibited a variability and are thus given as distributions (see Figure 7). Unless specified otherwise, the DEM

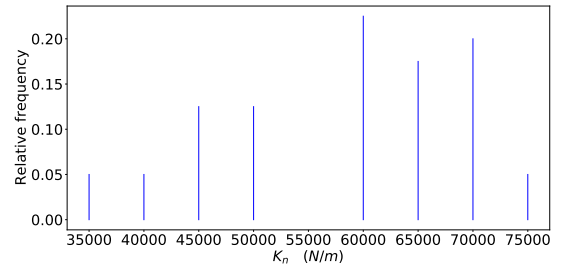
clump simulations are defined accordingly, assigning to all contacts random values of  $\varphi$  and  $c_n$  which respect the same distributions.



(a) Contact friction angles for particle/particle ( $\varphi_{p/p}$ ) or particle/wall ( $\varphi_{p/w}$ ) contacts



(b) Restitution coefficient



(c) Normal stiffness

**Fig. 7:** Distributions of contact properties as experimentally measured by the JGS (adapted from [4])

## 2.4 DEM simulation workflow

Building DEM samples starts with generating randomly in space particles inside the cuboidal or cylindrical containers mentioned in the above

### 3 Methodological discussion 413

#### 3.1 Computational aspects of each modelling approach 414

In order to provide an overlook of the computational implications of the two considered DEM strategies for shape description, Figure 8 gives a comparison of the computation performances observed during 30 different simulations with both modelling approaches, in terms of computation speed  $S$  and Cundall's number  $N_C = N_{part}S$ . These simulations, presented in more details in Section 4.3, were run sequentially using a Intel(R) Xeon(R) Platinum 8270 CPU @ 2.70GHz with 1.5 TB of RAM available. Note that during all series of simulations in this paper the CPU cache wasn't controlled. Its capacity of 35.75 MB may thus not have been used as much over all simulations, making the time measurements somewhat biased. 415

Note that heaps may reach equilibrium at different simulated times; as a consequence, less and less values were available to compute the mean and standard deviation, until eventually there was only one. The results show that for these simulations, the clump model is approximately 100 times faster than the potential particle model. Considering that the present physical particles are simple to describe in a clump approach, using only 4 416

Section 2.1, so as to form a extremely loose assembly of non-overlapping particles. The assembly is then deposited under its own weight until it becomes stable, and is saved to be subsequently used under different conditions. Different samples can be obtained starting from different initial particle arrangements. For this first step that has no experimental counterpart, an extra, non-physical, damping source is added in the local, non-viscous, form (Cundall's damping) to speed up the generation. For the rest of the simulations, contact-scale viscous damper and friction solely ensure the stabilisation of the simulations and no other source of damping is used. 417

The actual AOR simulation starts from this initial state by displacing the moving parts of the container in a manner equivalent to the experiments. Particles leaving the container from its periphery are counted as so-called lost particles and erased for computational efficiency. The simulation continues until the sample finds a new equilibrium in the form of a static heap. It is then possible to measure the angle between its exterior surface and the horizontal plane following the procedures discussed below. 418

The default set of parameters for this numerical setup is the experimental one previously given in Table 1. 419

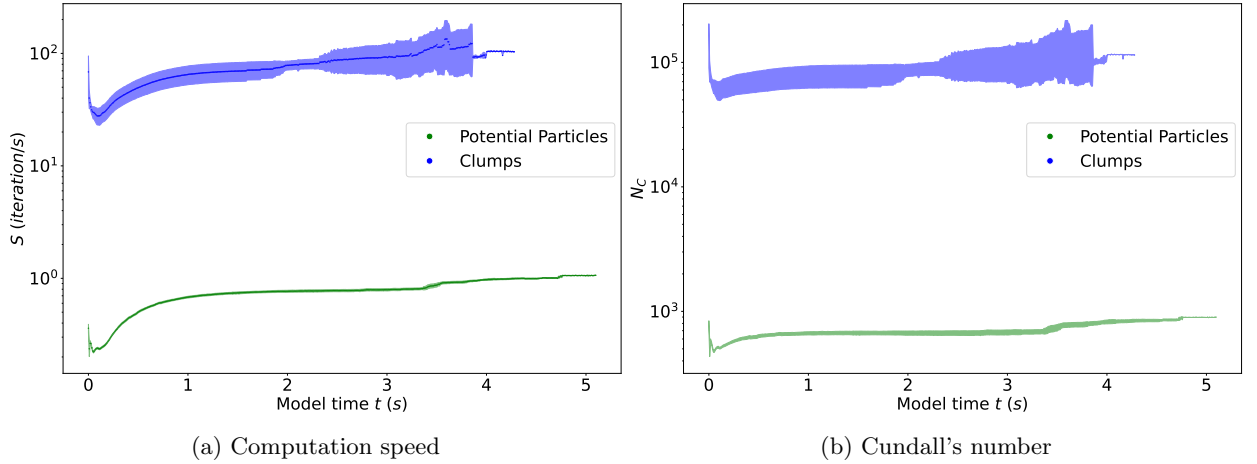


**Fig. 8:** Computation speed statistics during 30 simulations with each DEM approach (either potential particles or clump, see Section 4.3 for details). Dots represent the mean speed value with the surrounding filled area corresponding to its standard deviation.

441 spherical members, the increased effort in compu-  
 442 tational time when using potential particles is in a  
 443 classical order of magnitude for DEM approaches  
 444 for non-spherical particles [23].

### 445 3.2 A systematic determination of 446 the angle of repose

447 This section proposes two rigorous methods to  
 448 measure the AOR, first, by defining an outer sur-  
 449 face of particles and second, by computing an  
 450 angle from these particles positions.

#### 451 3.2.1 Outer surface detection

452 In the axisymmetric case (respectively plane strain  
 453 case), the 3D space is discretized in several subdo-  
 454 mains  $\{r; \theta \in [\theta_a, \theta_b]; z \in [z_a, z_b]\}$  (respectively  
 455  $\{x \in [x_a, x_b]; y \in [y_a, y_b], z\}$ ), giving an intersec-  
 456 tion with the outer surface at  $\max(r)$  (respectively  
 457  $\max(z)$ ) in each subdomain. The extent of each

interval is selected such that only one particle 458  
 should be therein detected as belonging to the 459  
 outer surface. For such a purpose, length scales  $L_\eta$  460  
 are used for the coordinates  $\theta, z$  in the axisymmet- 461  
 ric case and  $x, y$  in the plane strain case. The index 462  
 $\eta$  can represent each of these coordinates. The 463  
 number of intervals on each coordinate is then: 464

$$N_\eta = \frac{L_\eta}{d_{clump}} - 1 \quad (4)$$

with  $L_\theta = 2\pi R_{cyl}$ ,  $L_z = H_{cyl}$ ,  $L_x = L_{par}$ , and 465  
 $L_y = H_{par}$ . 466

$$\theta_a^i = i \frac{2\pi}{N_\theta}; \quad \theta_b^i = (i+1) \frac{2\pi}{N_\theta} \quad (5)$$

with  $i \in \llbracket 0; N_\theta \rrbracket$

$$\eta_a^i = i \frac{L_\eta}{N_\eta}; \quad \eta_b^i = (i+1) \frac{L_\eta}{N_\eta} \quad (6)$$

with  $i \in \llbracket 0; N_\eta \rrbracket, \eta \in \{x, y, z\}$

467 Figure 9 shows a typical result after detect-  
 468 ing all the particles belonging to the outer surface  
 469 in both configurations. Note that gravity has the  
 470 opposite orientation of the z-axis.

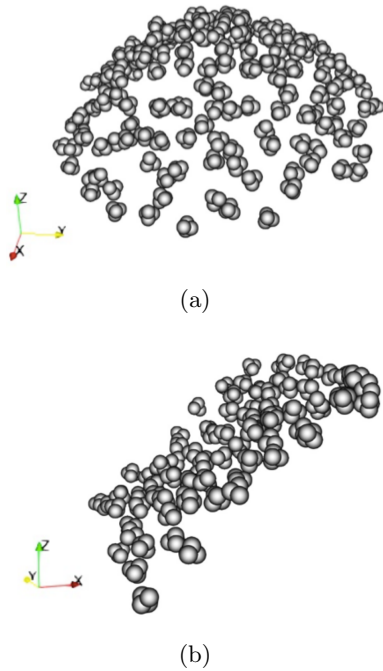


**Fig. 9:** Outer surface in the axisymmetric (a) and plane strain configurations (b).

in the plane strain case.

Assuming a  $\tilde{z}$ -invariance of the heaps, we project the spheres on the  $(\tilde{x}, \tilde{y})$  planes (see Figure 10) and perform a linear regression on the resulting points to determine the AOR  $\alpha$ . Letting the linear regression be  $\tilde{y}_1 = a_1\tilde{x} + b_1$ , one has:

$$\alpha = \arctan(a_1) \quad (7)$$

Consistently with [13, 14], one can notice that the surface isn't exactly flat but slightly curved (especially in the axisymmetric configuration). It can thus be useful to compute a second degree regression as well in order to fit the outer surface in the best possible way. Letting the second degree regression be  $\tilde{y}_2 = a_2\tilde{x}^2 + b_2\tilde{x} + c_2$ , one can compute a local angle:

$$\alpha(\tilde{x}) = \arctan(2a_2\tilde{x} + b_2) \quad (8)$$

To make the measurement more meaningful, one may naturally restrict the procedure to a smaller zone of the heap: the particles considered in the regressions would only be the ones inside an interval  $[\tilde{x}_{min}, \tilde{x}_{max}]$ . Indeed, the lower particles may be abruptly blocked by the bottom ridge of the container devices and should be excluded from the measurement. Also, particles with a high  $\tilde{x}$ , away from the opened boundary, could be unaffected by the discharge and still form a horizontal

### 3.2.2 Angle of repose measurement

From this point the method is the same in both heap configurations except for the orientation of the horizontal axis. The coordinates  $(\tilde{x}, \tilde{y}, \tilde{z})$  will thus denote respectively  $(-r, z, \theta)$  in the axisymmetric case or  $(x, z, y)$  in the plane strain case. The width of the container  $\tilde{x}_{box}$  for instance stands for  $R_{cyl}$  in the axisymmetric case and  $L_{par}$

504 surface, especially in the axisymmetric configura-  
 505 tion. Indeed, finite particle-size effects necessarily  
 506 exist and affect the transition from one side of the  
 507 slope to another.

508 Excluding from the bottom of the heap the  
 509 few particles that are stuck by the ridge, and only  
 510 those, is obtained choosing:  $\tilde{x}_{min} = 0.32d_{clump}$ .  
 511 An appropriate value for  $\tilde{x}_{max}$  is sought by mea-  
 512 suring  $\alpha$  for several  $\tilde{x}_{max}$ . The best  $\tilde{x}_{max}$  is the  
 513 smallest for which the measurement does not  
 514 change. The error on the measurement is also a  
 515 criterion to choose the best  $\tilde{x}_{max}$ . This method  
 516 should be specially relevant in the axisymmetric  
 517 case since the outer surface is curved, but it should  
 518 work on the plane strain heap as well.

### 519 3.2.3 Error on the measurement

520 For a given heap, the dispersion of positions data  
 521 induces some error on the linear regression and the  
 522 measurement of  $\alpha$ . As an alternative to the corre-  
 523 lation coefficient  $R^2$ , this error can be quantified  
 524 from a standard deviation on the slope  $a_1$  of the  
 525 fitting line,  $\text{StD}(a_1)$ . If  $N$  is the number of points  
 526 and  $(\tilde{x}_i, \tilde{y}_i)$  are the coordinates of the  $i^{th}$  point,  
 527 one has:

$$\text{StD}(a_1) = \sqrt{\frac{1}{N-2} \frac{\sum_{i=1}^N (a_1 \tilde{x}_i + b_1 - \tilde{y}_i)^2}{\sum_{i=1}^N (\tilde{x}_i - \bar{\tilde{x}})^2}} \quad (9)$$

(10)

which, considering Equation 7, gives the standard  
 deviation on the angle,  $\text{StD}(\alpha)$ :

$$\text{StD}(\alpha) = \frac{\text{StD}(a_1)}{1 + a_1^2} \quad (11)$$

528 Figure 10 shows the regressions made on the  
 529 projection of the outer surface in both configura-  
 530 tions and the resulting angle for  $\tilde{x}_{max}/\tilde{x}_{box} = 0.4$ ,  
 531 with  $\tilde{x}_{box} \in \{R_{cyl}, L_{par}\}$ . Figure 11 shows mea-  
 532 surements performed for several  $\tilde{x}_{max}$  in both  
 533 configurations. The error bars represent the error  
 534 computed with Equation 11. One can see that the  
 535 AOR increases with  $\tilde{x}_{max}$ , except for very high  
 536 values of  $\tilde{x}_{max}$  where the part of the outer sur-  
 537 face considered is very small compared to its size.  
 538 This may be caused by the ridge on the bottom  
 539 of the open container that maintains some parti-  
 540 cles, affecting the geometry of the outer surface.  
 541 The error on the measurement is very low but  
 542 increases with  $\tilde{x}_{max}$ . The measurement is more  
 543 stable for low  $\tilde{x}_{max}$ , specially in the axisymmet-  
 544 ric case. From now on, the measurements will be  
 545 performed on most of the outer surface, using  
 546  $\tilde{x}_{min} = 0.32d_{clump}$  and  $\tilde{x}_{max} = \tilde{x}_{box}$ .

### 547 3.2.4 Error due to repeatability

548 The simulations performed with the clump model  
 549 include two sources of randomness. The first one  
 550 is the initial configuration of the sample, with ran-  
 551 dom positions for the particles in the initial cloud.

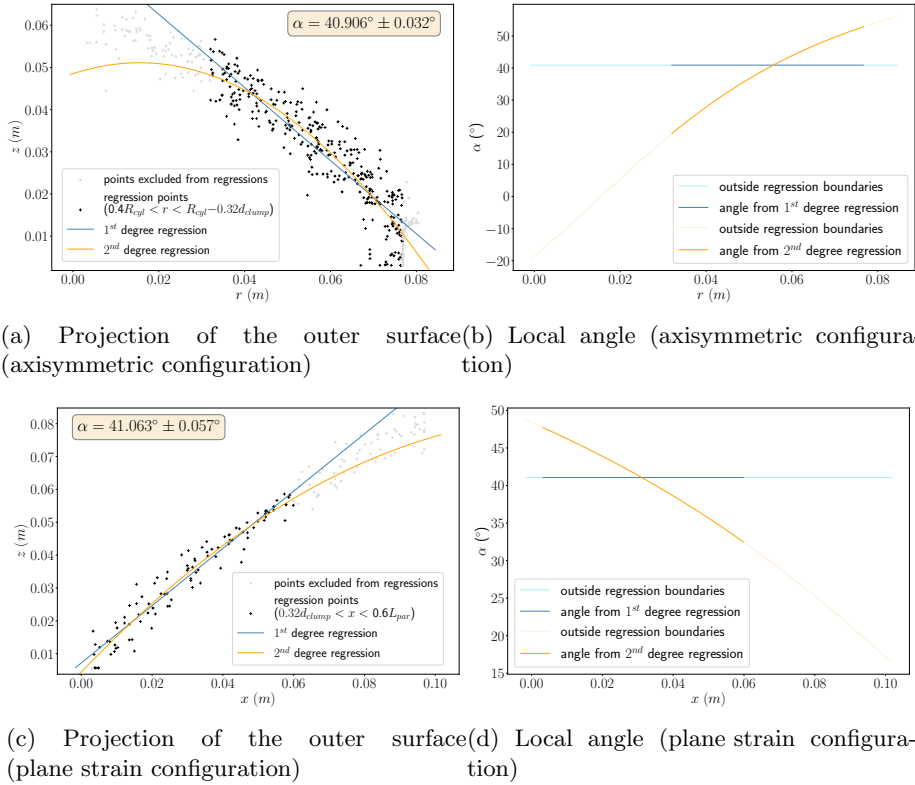


**Fig. 10:** Outer surface regressions for an intermediate  $\tilde{x}_{min}$  and the associated measurement ((a), (c)) in both configurations.

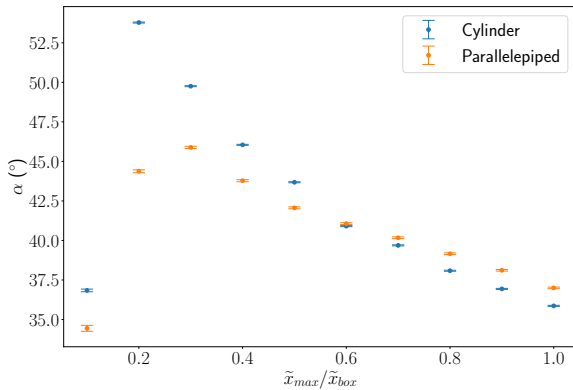


**Fig. 11:** Average slope as measured for different values of  $\tilde{x}_{max}$ .

implies choosing a different value for each contact, all values being randomly chosen according to the given probability distribution. If one was to swap the values of two contacts, the distribution would still be respected, but the conditions of the simulation would be different, introducing randomness.

In order to quantify the repeatability error, a series of simulations was performed with the clump model using 30 different values for the seed parameter, the particles in the initial samples of each simulation thus have different positions and contact properties. This series will be called

The second source lies in the statistical distribution of contact properties (see the above Figure 7). Indeed, the use of distributions for  $\varphi$  and  $e_n$

568 CLP1 and uses the default parameters of Table  
 569 4. Among those parameters, the time step is  
 570 computed from contact stiffnesses and particle  
 571 masses following [26]. Note that all samples have  
 572 approximately the same initial densities. Figure  
 573 12 shows the AOR measured using CLP1 heaps  
 574 and one can see that the variation in the mea-  
 575 surement is lower than 3%. Even though such a  
 576 repeatability error is low, it will be systematically  
 577 given for all series of simulations in this paper as  
 578 error bars on the AOR charts.

579

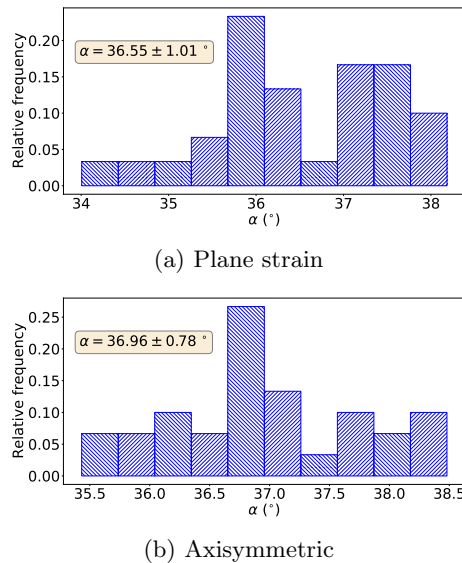


**Fig. 12:** Distributions of measured angles of repose when investigating repeatability in the CLP1 configurations of Table 4.

### 3.3 Measuring the void ratio for any geometry of assembly

582 With respect to the objective of discussing the  
 583 possible constitutive nature of the AOR deter-  
 584 mined as per Section 3.2, it is interesting to  
 585 characterize the state of the heap in terms of den-  
 586 sity or void ratio  $e$ , as a fundamental parameter  
 587 of granular materials. This density characteriza-  
 588 tion is not straightforward because of the irregular  
 589 geometry of the heap along its free surface, and  
 590 possible bias caused by an excess of void near the  
 591 walls

592 As such, two methods are proposed below to  
 593 compute the void ratio inside a granular assem-  
 594 bly with a complex geometry, while avoiding the  
 595 boundary effects: a so-called "tetrahedra method"  
 596 and a "sub-volume method". Both methods pro-  
 597 vide local values for  $e$  and rely on a Monte Carlo  
 598 procedure to compute volume proportions, com-  
 599 bined with (straightforward, here) tests to deter-  
 600 mine whether a random point in space is inside  
 601 a physical particle. The following differences still  
 602 exist, though:

- 603 • the tetrahedra method applies for any geom-  
 604 etry of sample with no requirements on the  
 605 geometry. It is based on a triangulation of the  
 606 sample.
- 607 • the sub-volume method requires to define  
 608 an homothetic sub-volume inside the sample,

**Table 4:** Parameters for heap simulations investigating repeatability (CLP1 series, 60 simulations in total).

Configuration	$N_{part}$	$\frac{K_n}{(N.m^{-1})}$	$K_s/K_n$	$\frac{\rho}{(kg.m^{-3})}$	$\Delta t$ (s)	$\varphi$	$e_0$	Number of samples
Plane strain	2,150	58,250	0.37	1,111	$7.86 \times 10^{-5}$	see	$0.622 \pm 0.012$	30
Axisymmetric	2,468					Figure 7	$0.744 \pm 0.028$	

which can be difficult if the latter adopts a peculiar geometry. However, it is substantially faster than the tetrahedra method.

### 3.3.1 The tetrahedra method

In order to compute a void ratio on a heap with a random geometry, the tetrahedra method starts by a triangulation of the heap. The Monte Carlo method is then used to determine the proportion of particles inside each tetrahedron resulting from the triangulation, leading to an expression for the void ratio.

#### 3.3.1.1 Triangulating the heap

This first step is done using Delaunay's triangulation on the centers of all particles, although it could be done using another set of relevant points (e.g. the center of all spheres for clump simulations). Also, one should keep in mind that when triangulating using the center of the particles a small part of the sample is ignored: all particles on the outer surfaces are cut by the boundary tetrahedra. This should effectively remove the excess of

void near the walls of any sample. The set of all tetrahedra will be denoted  $\{tet\}$ .

#### 3.3.1.2 Detecting which particle may be partially inside each tetrahedron

All particles bounding boxes are tested to determine if they overlap a tetrahedron bounding box. If so, the particle is further checked for intersected volume with the Monte Carlo method, forming a set of particles that is denoted  $\{p\}^{cut}$ . This step is not mandatory but it drastically reduces the computation time.

#### 3.3.1.3 Computing the total volume of particle inside each tetrahedron

In this final step,  $N_{mc}$  points  $\{\underline{x}_i, i \in [1, N_{mc}] \cap \mathbb{N}\}$  are uniformly drawn inside the tetrahedron, following [27]. Each point is tested to determine if it is located inside any of the particles potentially cut  $\{p\}^{cut}$ . Denoting  $V^{tet}$  the volume of a tetrahedron  $tet$  computed using its vertices' coordinates;  $\chi^p(\underline{x})$  the Boolean test function equal to

656 1 if the point  $\underline{x}$  is inside the particle  $p$ , 0 otherwise;  
 657 and  $H(n)$  the Heaviside function, the Monte-Carlo  
 658 method gives the total volume of particle inside  
 659 the tetrahedron as follows:

$$V_{part}^{tet} = \frac{\sum_{i=1}^{N_{mc}} H\left(\sum_{\{p\}^{cut}} \chi^p(\underline{x}_i)\right)}{N_{mc}} \times V^{tet} \quad (12)$$

660 A local void ratio can then be computed for  
 661 the tetrahedron:

$$e^{tet} = \frac{V^{tet} - V_{part}^{tet}}{V_{part}^{tet}} \quad (13)$$

And globally:

$$V_{part} = \sum_{\{tet\}} V_{part}^{tet} \quad (14)$$

$$V_{tot} = \sum_{\{tet\}} V^{tet} \quad (15)$$

$$e = \frac{V_{tot} - V_{part}}{V_{part}} \quad (16)$$

662 Taking advantage of the independence between  
 663 operations in each tetrahedron, the proposed  
 664 implementation of this method is parallel with an  
 665 almost optimal speed-up: the increase in execution  
 666 speed is close to the number of processes running  
 667 at the same time.

668

### 669 3.3.2 The sub-volume method

670 The sub-volume method consists in three steps  
 671 detailed below.

#### 3.3.2.1 Defining the sub-volume

672

673

674

This step is illustrated using the two samples' geometries considered in this paper. The sub-volume is chosen as a homothetic transformation of the heap centered in the sample, for both configurations. The sub-volume and the total volume of the sample will be denoted  $V_{sub}$  and  $V$ , respectively. At the final state, the geometry of the sample is assumed to be a half parallelepiped (respectively a cone) for the plane strain (respectively axisymmetric) configuration. The sub-volume is defined using a parameter  $C$  that pilots the homothetic transformation. The coordinates of the sub-volume axis aligned bounding box are denoted  $(x_{min}, y_{min}, z_{min})$  and  $(x_{max}, y_{max}, z_{max})$  and depend on the coordinates of the sample axis aligned bounding box:  $(X_{min}, Y_{min}, Z_{min})$  and  $(X_{max}, Y_{max}, Z_{max})$ .

675

676

677

678

679

680

681

682

683

684

685

686

687

688

689

690

691

In the case of the plane strain configuration, the homothetic sub-volume can be determined as follows (Figure 13):

692

693

694

$$s_{min} = (1 - C)(S_{max} - S_{min}) + S_{min} \quad (17)$$

$$s_{max} = C(S_{max} - S_{min}) + S_{min} \quad (18)$$

with  $\forall (s, S) \in \{(x, X), (y, Y), (z, Z)\}$  and  $\forall C \in ]0.5, 1]$ .

695

696

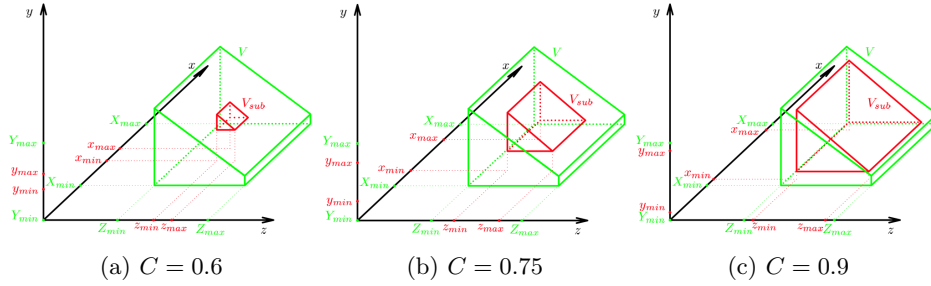


**Fig. 13:** Illustration of sub-volume for several  $C$  values in the plane strain configuration.

697 In the case of the axisymmetric configuration,  
 698 one has to compute the  $x$  and  $y$  coordinates of the  
 699 center,  $x_\Omega$  and  $y_\Omega$  respectively, and the maximum  
 700 radius  $r_c$  of the cone (Figure 14). The homothetic  
 701 sub-volume is then:

$$z_{min} = (1 - C)(Z_{max} - Z_{min}) + Z_{min} \quad (19)$$

$$z_{max} = C(Z_{max} - Z_{min}) + Z_{min} \quad (20)$$

$$s_\Omega = \frac{S_{min} + S_{max}}{2} \quad (21)$$

$$r_c = (2C - 1) \frac{X_{max} - X_{min} + Y_{max} - Y_{min}}{4} \quad (22)$$

702 with  $\forall (s, S) \in \{(x, X), (y, Y)\}$  and  $\forall C \in ]0.5, 1]$ .

### 703 3.3.2.2 Counting the volume of particles 704 completely inside the sub-volume

705  
 706  
 707 During this step, the 8 vertices  $\underline{x}_i^p$  of a particle  
 708 axis aligned bounding box are tested to deter-  
 709 mine if they are part of the sub-volume. Using the

$\chi^{sub}(\underline{x})$  function, the number of vertices inside the  
 710 sub-volume for a particle  $p$  reads:  
 711

$$N_{in}^p = \sum_{i=1}^8 \chi^{sub}(\underline{x}_i^p) \quad (23)$$

If  $N_{in}^p = 8$ , the particle  $p$  is completely inside  
 712 the sub-volume while if  $N_{in}^p = 0$  the particle  $p$  is  
 713 completely outside the sub-volume.  
 714

Denoting  $V^p$  the volume of the particle  $p$ , the  
 715 total volume of particles completely inside the  
 716 sub-volume is:  
 717

$$V_{part}^{in} = \sum_{\{p \mid N_{in}^p=8\}} V^p \quad (24)$$

### 718 3.3.2.3 Counting the volume of particles 719 partially inside the sub-volume

720  
 721  
 722 If  $0 < N_{in}^p < 8$ , the particle may be cut by  
 723 the faces of the sub-volume. The proportion of  
 724 the particle volume inside the sub-volume is again  
 725 determined using the Monte Carlo method:  $N_{mc}$   
 726 points,  $\{\underline{x}_i, i \in \llbracket 1; N_{mc} \rrbracket\}$ , are uniformly drawn  
 727 inside the particle bounding box and tested to

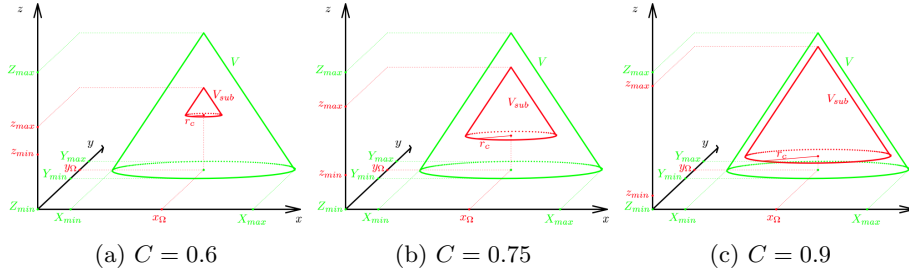


**Fig. 14:** Illustration of sub-volume for several  $C$  values in the axisymmetric case.

728 determine if they are simultaneously inside the  
 729 sub-volume (test function  $\chi^{sub}(\underline{x}_i)$ ) and inside the  
 730 particle (test function  $\chi^p(\underline{x}_i)$ ). The proportion of a  
 731 particle volume being also part of the sub-volume  
 732 is then:

$$V_{in}^p = \frac{\sum_{i=1}^{N_{mc}} \chi^{sub}(\underline{x}_i) \chi^p(\underline{x}_i)}{N_{mc}} \times V^p \quad (25)$$

733 The total volume of particles partially inside  
 734 the sub-volume is:

$$V_{part}^{cut} = \sum_{\{p \mid 0 < N_{in}^p < 8\}} V_{in}^p \quad (26)$$

735 The total volume of particle inside the sub-  
 736 volume then reads:

$$V_{part} = V_{part}^{in} + V_{part}^{cut} \quad (27)$$

737 Finally, the void ratio is determined by:

$$e = \frac{V_{sub} - V_{part}}{V_{part}} \quad (28)$$

For the simplest sub-volume geometries the  
 expression of  $V_{sub}$  is trivial. In more complex sit-  
 uations it can be determined using once again  
 the Monte Carlo method inside the sub-volume  
 bounding box:

$$V_{sub}^{bb} = (x_{max} - x_{min})(y_{max} - y_{min})(z_{max} - z_{min}) \quad (29)$$

$$V_{sub} = \frac{\sum_{i=1}^{N_{mc}} \chi^{sub}(\underline{x}_i)}{N_{mc}} \times V_{sub}^{bb} \quad (30)$$

Both methods can be optimized when used  
 with simple shapes (e.g. spheres): one could detect  
 more precisely which particle may be cut. Also,  
 one may be able to draw uniformly points directly  
 inside the particle instead of the bounding box,  
 making it possible to set aside the function  $\chi^p$  and  
 giving a more accurate Monte Carlo method.

### 3.3.3 Examples of void ratio

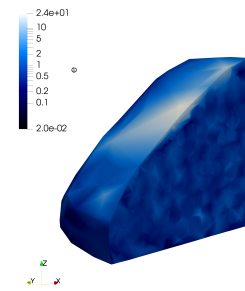
#### measurements

#### 3.3.3.1 Local void ratio

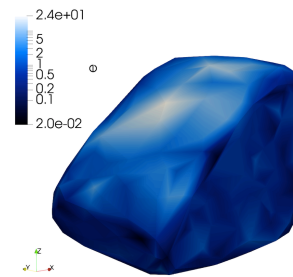
The tetrahedra method makes it possible to establish directly a local representation of the void ratio, as illustrated in Figure 15 for one plane strain final heap. One can notice that the geometry of the final heap is accurately captured by the triangulation, giving a rounded half parallelepipedic boundary surface. The density range is quite wide: some tetrahedra located on the outer surface, where the particles moved, contain approximately 1000 times more voids than other tetrahedra located where the particles almost didn't move. Note that this figure represents the void ratio directly interpolated from the centroids of each tetrahedron and thus should be interpreted carefully.

#### 3.3.3.2 Parallel implementation of the tetrahedra method

The independence of the processing of each tetrahedron makes it possible to parallelize this method. A series of measurements was performed on 30 clump samples at their initial states (showing different individual locations of particles)



(a) Sliced view



(b) Complete view

**Fig. 15:** Local void ratio in a plane strain final heap as measured with the tetrahedra method.

using different numbers of CPU cores,  $N_{cores} \geq 1$ , on the same machine previously used in Section 3.1. The speed-up  $S$  and its standard deviation  $\Delta S$  was computed from the computation times  $T_{N_{cores}} \pm \Delta T_{N_{cores}}$  as follows:

$$S = \frac{T_1}{T_{N_{cores}}} \quad (31)$$

$$\Delta S = S \left( \frac{\Delta T_1}{T_1} + \frac{\Delta T_{N_{cores}}}{T_{N_{cores}}} \right) \quad (32)$$

Since the CPU cache was not precisely controlled, the total CPU load had an influence on the computation speed, which might lead to a speed-up seemingly above perfection in the eventuality of

the CPU cache being full during the measurement on 1 core and not for more cores.

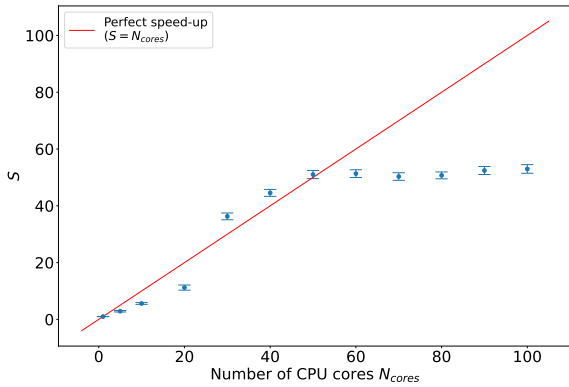


**Fig. 16:** Parallelization speed-up for the tetrahedra method.

Figure 16 shows the speed-up for  $N_{cores} \in \{1, 5, 10, 20, 30, 40, 50, 60, 70, 80, 90, 100\}$ . The speed-up stops to improve starting from  $N_{cores} = 50$ , which is probably due to an over usage of the CPU. A better control of the CPU could give more accurate speed-up measurements. Nevertheless, for  $N_{cores} < 50$  the parallelization is optimum:  $S \approx N_{cores}$ .

### 3.3.3.3 Sub-volume and tetrahedra methods comparison

Void ratio measurements were performed for the clump model on all 30 initial samples of CLP1 plane-strain series of simulations, discussed in more details in Section 4.3. Because of the

simple parallelepipedic geometry of these granular assemblies, a reference void ratio can be easily computed using the sample bounding box:

$$V_{tot} = (X_{max} - X_{min})(Y_{max} - Y_{min})(Z_{max} - Z_{min}) \quad (33)$$

$$V_{part} = \sum_{\{p\}} V^p, \text{ with } \{p\} \text{ the set of all particles} \quad (34)$$

$$e^{REF} = \frac{V_{tot} - V_{part}}{V_{part}} \quad (35)$$

Figure 17 (a) illustrates the comparison between the mean values and standard deviation over the 30 samples of  $e^{REF}$  together with  $e^{TET}$  for the tetrahedra method and  $e^{SUB}$  for the sub-volume method. The latter has been computed for 3 values of  $N_{mc}$  and 40 values of  $C$ .

For the lowest values of  $C$ , the measured  $e^{SUB}$  void ratio varies a lot among the 30 simulations and in function of  $N_{mc}$ . Between  $C \approx 0.7$  and  $C \approx 0.9$ ,  $e^{SUB}$  is constant and its standard deviation gets lower, being furthermore little dependent on  $N_{mc}$ . For  $C > 0.9$ , its mean value and standard deviation finally start to increase as expected due to the rigid boundaries constraining the granular assembly and favoring voids to form near the outer surfaces. Finally, for  $C = 1$ , the sub-volume method gives by definition the exact same values for void ratio than when using the global bounding box:  $e^{SUB} = e^{REF}$ .

828 The tetrahedra method gives a  $e^{TET}$  measure-  
 829 ment being close to  $e^{SUB}$  when  $0.7 < C < 0.9$ ,  
 830 which suggests that it successfully excludes the  
 831 excess of void from the computation.

832 As for the computational costs, Figure 17 (b)  
 833 shows the corresponding execution times,  $t^{SUB}$ ,  
 834  $t^{TET}$  and  $t^{REF}$ , while  $e^{TET}$  was computed using  
 835 parallelization on 3 cores. One observes that, in  
 836 spite of parallelization, the tetrahedra method  
 837 is here significantly slower than the sub-volume  
 838 method. Regarding the sub-volume method, using  
 839  $N_{mc} = 1000$  instead of  $N_{mc} = 100$  slows down  
 840 considerably the computation for no gain in accu-  
 841 racy, especially for high values of  $C$ .

842 In view of these results, subsequent measure-  
 843 ments of void ratio will be obtained using the  
 844 sub-volume method with  $N_{mc} = 100$  and  $C = 0.8$ .

## 845 4 Physical discussion

846 This section analyses the dependence of AOR on  
 847 several parameters: the particle shape, the ini-  
 848 tial void ratio and the sample size. Experimental  
 849 results obtained in [4] are also provided.

### 850 4.1 Parametric study

#### 851 4.1.1 (Non-)Sensitivity to the 852 tangential stiffness

853 A first series of simulations investigates the role of  
 854 tangential stiffness when using the potential par-  
 855 ticles model and two different values of  $K_s$ : 240  
 856  $N/m$  and 444  $N/m$  (see sets B and C of Table 5).

857 Results are given in Figure 18 for what con-  
 858 cerns the initial and final states of the samples.  
 859 Most importantly, the two different values of tan-  
 860 gential stiffness are shown to result in virtually  
 861 the same AOR distribution. The  $K_s = 240 N.m^{-1}$   
 862 value will thus be kept in the remainder of the  
 863 sequel for it results in a higher critical time step.  
 864 One may furthermore note that the initial coor-  
 865 dination number is slightly lower with a higher  
 866  $K_s$ , which is expected since stiff particles tend to  
 867 be further away from each other, even when con-  
 868 strained. However, at the final state, the average  
 869 coordination number is unaffected by  $K_s$ , cer-  
 870 tainly because they are not constrained enough for  
 871 their relative distance to depend on  $K_s$ .

#### 872 4.1.2 (Non-)Sensitivity to the particle 873 mass density

874 While the AOR  $\alpha$  refers to a static condition, the  
 875 mass density of particles  $\rho$  physically affects the  
 876 prior dynamic evolutions of the system. On the  
 877 other hand, from a computational standpoint, the  
 878 density also controls the critical time step of the

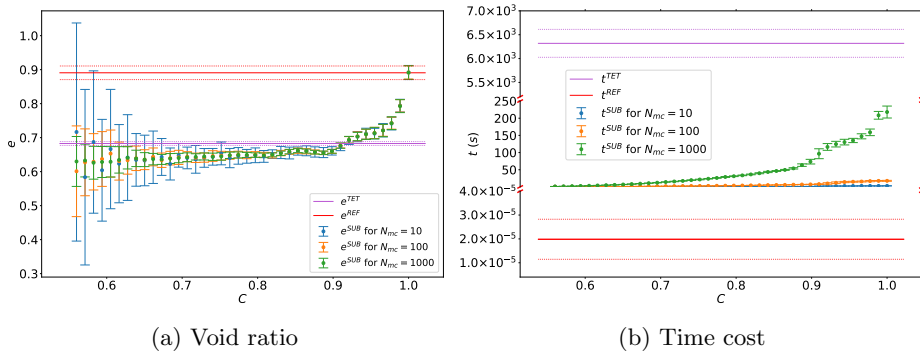


**Fig. 17:** Void ratio measurements with both methods for 30 parallelepipedic initial samples differing in individual locations of particles. On figure (b), the  $y$  axis is broken at two places: first between 40  $ns$  and 50  $ms$ , and second between 250  $s$  and 5200  $s$ . The three parts of the  $y$  axis do not have the same scale.

**Table 5:** Used parameters for the parametric study with potential particles - series PP1.

Set id	Configuration	$K_n$ ( $N.m^{-1}$ )	$K_s/K_n$	$\rho$ ( $kg.m^{-3}$ )	$\Delta t$ (s)	$\varphi_{p/p}$ ( $^\circ$ )	$\varphi_{p/w}$ ( $^\circ$ )	$\beta_n$	Number of samples
A	Plane strain	1,200	0.2	1111	$8.52 \times 10^{-5}$	35.5	27.2	0.071	30
B			0.2	943	$7.86 \times 10^{-5}$				
C			0.37	943	$7.86 \times 10^{-5}$				

879 present explicit DEM scheme and the total time  
 880 cost. Other series of simulations with different  $\rho$   
 881 are thus proposed to check whether a variation  
 882 from the experimental reference  $\rho = 1,111 \text{ kg/m}^3$   
 883 would affect the AOR results.

884 Using potential particles, two values for the  
 885 particle density are considered in the framework  
 886 of the PP1 series (sets A and B of Table 5):  
 887 the experimental one,  $\rho = 1,111 \text{ kg/m}^3$ , and  
 888  $\rho = 943 \text{ kg/m}^3$  that would confer the potential  
 889 particle the same mass as the physical parti-  
 890 cle in spite of the volume differences discussed  
 891 in the above Section 2.2.3. Using clumps in a  
 892 CLP2 series, four to seven different values for  
 893  $\rho \in [100 \text{ kg/m}^3; 10,000 \text{ kg/m}^3]$  are considered,  
 894 with 10 different initial samples in each case.

895 Corresponding parameters are all given in Table  
 896 6.

897 Figure 19 shows the resulting angles of repose  
 898 in the CLP2 and PP1 series, together with time  
 899 costs of CLP1 series measured for a sequential  
 900 execution on the same machine presented in previ-  
 901 ous Section 3.1. The dots correspond to the mean  
 902 measurement over all samples for a given particle  
 903 density and the error bars represent the standard  
 904 deviation. One can see that all error bars share  
 905 a common zone for a given shape description. As  
 906 such, it is herein concluded, consistent to [9], that  
 907 particle density does not impact the AOR. During  
 908 DEM simulations, one can thus adopt, when nec-  
 909 essary, an artificial  $\rho = 10,000 \text{ kg/m}^3$ , multiplying  
 910 the critical time step by a factor of  $\sqrt{\frac{10000}{1111}} \approx 3$

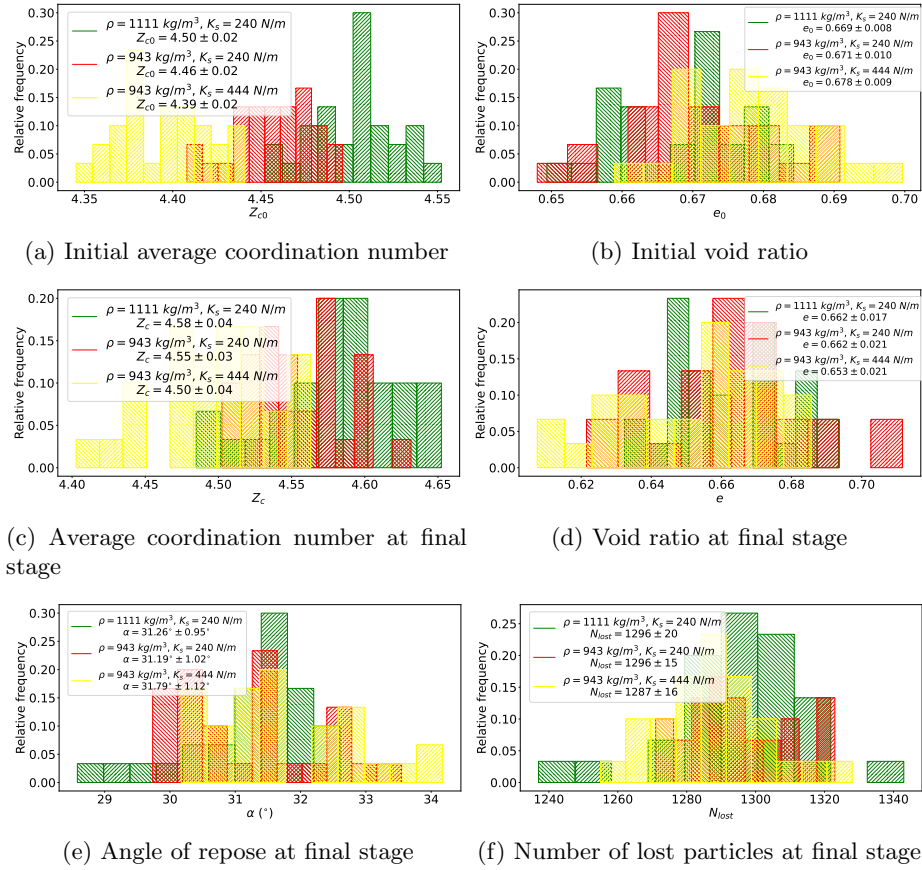


**Fig. 18:** Macro-scale and micro-scale results of the parametric analysis with potential particles (PP1 series, Table 5).

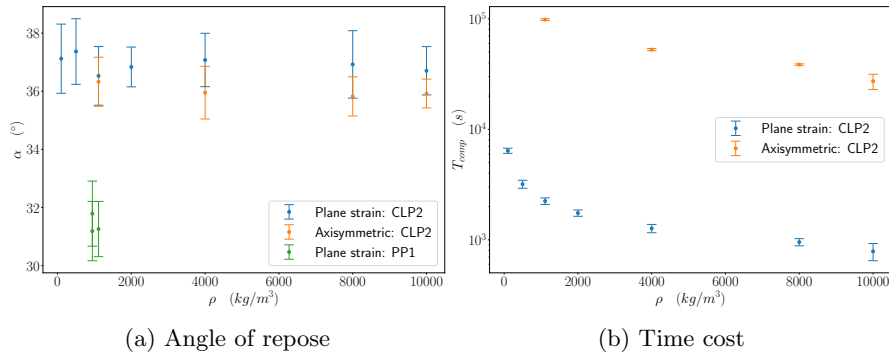


**Fig. 19:** Particle density influence on the angle of repose and on the time cost - CLP2 and PP1 series

911 and reducing as much as possible the total time cost of the  
912 simulation (Figure 19b) until the heap stabilizes.

913 In the Figure 19b, one can finally note a longer

914 computation time for the axisymmetric configuration

915 because of a lower velocity of the descending

916 wall in the reference experiments.

**Table 6:** Parameters of heap simulations investigating  $\rho$  influence (CLP2 series, 110 simulations in total).

Configuration	$N_{part}$	$\rho$	$\epsilon_0$	Number of samples
Plane-strain	2,150	100 $kg/m^3$	$0.652 \pm 0.011$	10
		500 $kg/m^3$	$0.633 \pm 0.010$	
		1,111 $kg/m^3$	$0.623 \pm 0.009$	
		2,000 $kg/m^3$	$0.618 \pm 0.010$	
		4,000 $kg/m^3$	$0.607 \pm 0.011$	
		8,000 $kg/m^3$	$0.603 \pm 0.012$	
Axisymmetric	2,468	10,000 $kg/m^3$	$0.603 \pm 0.010$	
		1,111 $kg/m^3$	$0.743 \pm 0.022$	
		4,000 $kg/m^3$	$0.723 \pm 0.015$	
		8,000 $kg/m^3$	$0.709 \pm 0.019$	
		10,000 $kg/m^3$	$0.694 \pm 0.010$	

## 4.2 Numerical angle of repose vs experimental one

The numerical simulations are now compared with the experimental results provided at the end of the JGS round-robin and in [4]. In this framework, a simpler method was adopted to compute the AOR, considering only the highest particle instead of the whole external surface as in previous Section 3.2, for sake of simplicity during the experiments. In the axisymmetric configuration, slopes are actually determined in 360 directions being not exactly radial and their average is used to compute the AOR, while in the plane strain configuration the AOR is computed using only one slope direction in the plane.

In this subsection, the exact same method is adopted to interpret our numerical results for a consistent comparison. The set of parameters used for the clump model is the same as for CLP1 (see Table 4), and the set of parameters used for the potential particle model is given in Table 7.

Table 8 compares the obtained experimental and numerical results. In the plane strain configuration, the experimental AOR is approximately 8% higher than the one obtained for the clump model and 16% higher than the one obtained for the potential particle model. In the axisymmetric configuration, the experimental AOR is approximately 4% higher than the one obtained with the clump model and 16% higher than the one obtained for the potential particle model. Also, one should notice that in the plane strain configuration the JGS method measures an AOR higher than the method presented in this paper, and lower in the axisymmetric configuration (see Figure 12). This changes the conclusion on the influence of the configuration: with our measurement method both configurations gives the same AOR (difference of approximately 1% with the clump model), while the JGS method gives a difference of approximately 11%.

**Table 7:** Material properties used in the potential particles models.

$K_n$ ( $N.m^{-1}$ )	$K_s/K_n$	$\rho$ ( $kg.m^{-3}$ )	$\Delta t$ (s)	$\varphi_{p/p}$ ( $^\circ$ )	$\varphi_{p/w}$ ( $^\circ$ )	$\beta_n$
1200	0.773	943	$7.86 \times 10^{-5}$	35.5	27.2	0.071

**Table 8:** Angle of repose as per the JGS measurement method.

	Number of samples	Average ( $^\circ$ )	Standard Deviation ( $^\circ$ )	Minimum ( $^\circ$ )	Maximum ( $^\circ$ )
Plane strain configuration					
Experiments [4]	400	41.4	1.28	38.3	46.3
Clumps	100	38.1	1.14	35.0	41.3
Potential particles	18	34.8	1.61	32.5	38.0
Axisymmetric configuration					
Experiments [4]	50	35.3	0.9	33.3	37.3
Clumps	100	33.9	0.8	32.0	36.1
Potential particles	19	29.7	0.78	28.5	31.2

### 4.3 Role of particle concavity

The differences in AOR observed in Table 8 between the clump and potential particle (PP) models, with a higher discrepancy for PP towards experiments, certainly arise from the convex simplification of potential particles, with respect to the concavities of the physical particles which allow them to interlock better. In order to gain more insights into the influence of particle concavity, a rigorous comparison between the two numerical models is led in this subsection, adopting the same parameters for both models (except for the time step for computational efficiency) and determining the AOR using the more reliable method presented in Section 3.2. This series

is called PP-CLP, with all parameters being listed in Table 9 and Table 10.

Figure 20 characterizes the initial and final states of these PP-CLP simulations. First and foremost, it is to notice that the AOR is approximately 14% lower with the potential particle model. This difference can be considered as significant and is even greater with respect to experiments even though the physical particles show a fairly high convexity of 0.954. In line with additional possibilities of interlocking for non-convex particles, while convex particles fall more easily from the heap, the number of lost particles is approximately 23% lower with the clump model. One can also note that the final void ratio is approximately the same with both models and

**Table 9:** Contact parameters of the PP-CLP series focusing on particle concavity

Model	$K_n$	$K_s$	$e_n$	$\varphi_{p/p}$	$\varphi_{p/w}$
Clump Potential particle	$1.2 \text{ kN.m}^{-1}$	$0.24 \text{ kN.m}^{-1}$	0.8	$35.5^\circ$	$27.2^\circ$

**Table 10:** Other simulation parameters of the PP-CLP series on particle concavity

Model	Configuration	$\rho$	$\Delta t$	Number of samples
Clump Potential particle	Plane strain	$1111 \text{ kg.m}^{-3}$	$\approx 78.5 \mu\text{s}$ $\approx 85.2 \mu\text{s}$	30

that the final average number of contact points per particle is approximately 25% lower with the potential particle model since two convex particles can form only one contact point, unlike the concave clump.

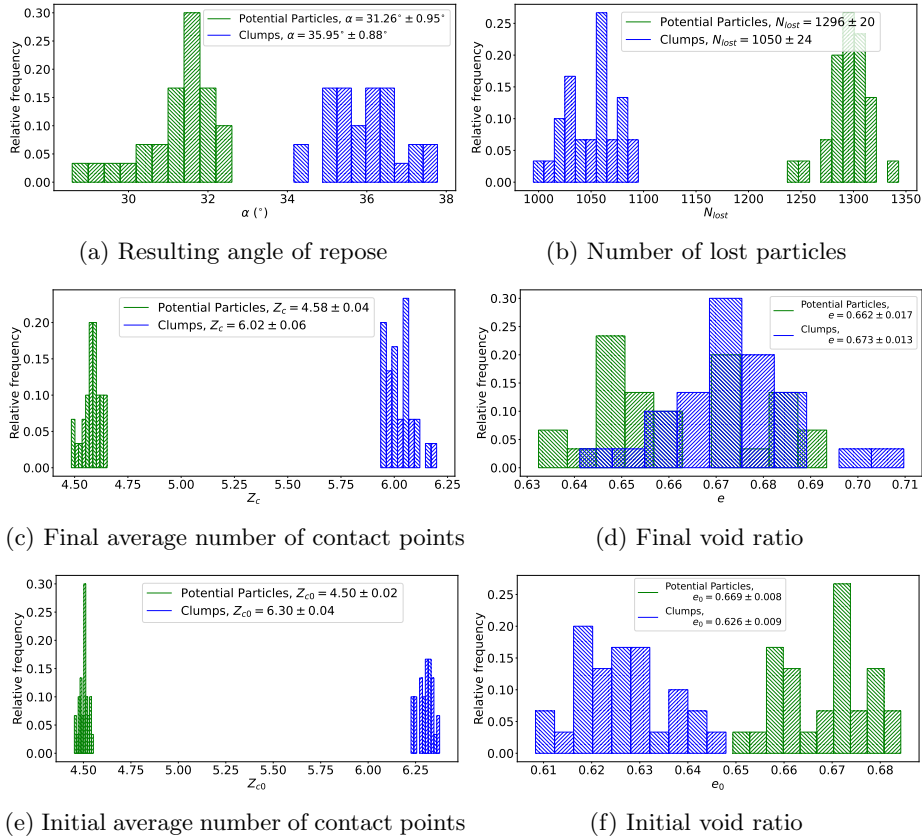
It is worth noticing that the experimental measurement method gives a gap between the axisymmetric and plane strain configurations' angle of repose. The curvature of the axisymmetric heap explains the lower measurement obtained with the JGS method.

Looking at initial stages, one observes that the initial void ratio is approximately 5% lower with the clump model. The difference between the void ratio at the initial state and final state is interesting: at the initial state the sample is constrained by four side walls and one bottom wall, while at the final state one of the four sides of the sample is free. This suggests that concave particles are more likely to fill the voids when they are surrounded by walls (parallel to the gravity axis), but when

they are free to move, they do not fill the voids better than convex particles. On the other hand, the difference on the average number of contact points is approximately the same at the initial and final states.

#### 4.4 (Non-)Constitutive nature of the angle of repose

The compatibility of AOR values measured (with the present method, see Figures 12 and 19) in both axisymmetric and plane strain configurations of the reference device could confirm a constitutive nature of the AOR inferred in, e.g., [5, 6, 7], suggesting to compare the latter with shear strength properties of the granular material. Generally speaking in solid-like granular mechanics, these shear strength properties may refer either to a critical state or a state of maximum stress ratio, the two being possibly different depending on initial porosity.

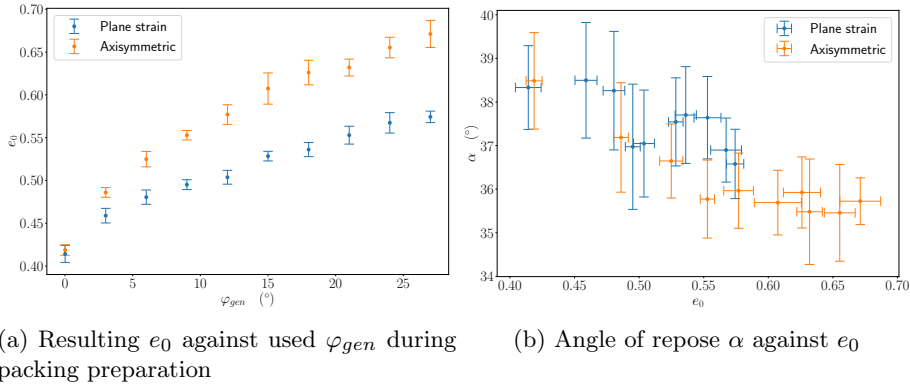


**Fig. 20:** Characterization of the PP-CLP series on particle concavity in terms of initial and final states

1029 Here, it is first determined whether the AOR  
 1030  $\alpha$  evolves with respect to the initial void ratio  $e_0$ ,  
 1031 which would contradict the definition of a crit-  
 1032 ical state property. This is done by performing  
 1033 a “CLP4” series of simulations with the clump  
 1034 model using several samples at different initial  
 1035 porosities, whose parameters are given in Table 11.  
 1036 The initial void ratio  $e_0$  is controlled by momen-  
 1037 tarily altering the inter-particle friction angle dur-  
 1038 ing the generation of the sample,  $\varphi_{gen}$ , whereby  
 1039 lower  $\varphi_{gen}$ -values lead to denser packings, as plot-  
 1040 ted in Figure 21 (a) where the error bars represent

1041 the standard deviation of  $e_0$  on all 10 simula-  
 1042 tions performed at the same  $\varphi_{gen}$ . Figure 21 (b)  
 1043 shows  $\alpha$  against  $e_0$  and reveals some decreasing  
 1044 tendency of  $\alpha$  for  $e_0 < 0.55$  in both configurations  
 1045 that would be more consistent with an interpreta-  
 1046 tion of the AOR in terms of a porosity-dependent  
 1047 maximum friction angle. However, the significant  
 1048 dispersion of the results prompts the need for  
 1049 further investigations in the following.

1050 In addition, it is to note that a critical state  
 1051 interpretation of the repose would impose a cor-  
 1052 relation between critical state values of porosity  
 1053 (or void ratio) and mean pressure  $p$  in the form

**Fig. 21:** Influence of the initial void ratio  $e_0$  - CLP4 series

1054 of a critical state line (CSL). Assuming, likewise  
 1055 to void ratio  $e$ , that an average (i.e. global) stress  
 1056 tensor is a meaningful quantity to characterize the  
 1057 heap in spite of gravity, the Appendix B recalls  
 1058 the expression of the latter tensor and the cor-  
 1059 responding mean stress  $p$  in Equation B17. The  
 1060 final states  $(e, p)$  of a large set of 400 heaps simu-  
 1061 lated in the previous series CLP1, CLP4 together  
 1062 with a forthcoming CLP5 (grouped under a CLPX  
 1063 notation) are then compared in Figure 22 with the  
 1064 CSL of the present granular material, previously  
 1065 determined in [28] from DEM triaxial tests. The  
 1066 latter were performed in quasi-static conditions  
 1067 with a constant lateral stress in two directions and  
 1068 an imposed a strain rate in the third direction.  
 1069 Each of the 105 triaxial tests plotted on Figure  
 1070 22 contained 7,500 clumps, which was shown to  
 1071 be enough to constitute a REV for the study  
 1072 of the material stress-strain behaviour. The crit-  
 1073 ical state was observed to be attained when the

axial strain  $\epsilon_{ax}$  reaches 0.6, i.e. both the devia- 1074  
 toric stress and volumetric strain were unaffected 1075  
 by further deformations. Any critical state quan- 1076  
 tity is thus computed as an average of its value 1077  
 over  $\epsilon_{ax} \in [0.6, 0.8]$ . It is to note that it was 1078  
 shown in [28] to be more relevant to consider rat- 1079  
 tlers (particles having at most 1 contact) as voids 1080  
 when determining the CSL of a granular mate- 1081  
 rial, to avoid an unphysical increase of the CSL 1082  
 in the  $(e, p)$  plane for low  $p$ . This is especially 1083  
 important here since body weights are the only 1084  
 external forces present in the CLPX series, making 1085  
 the average mean stress possibly quite low ( $\approx 100$  1086  
 $Pa$ ), depending on mass density. 1087

From the comparison in Figure 22, one can 1088  
 first note that the mechanical states in the CLPX 1089  
 series regroup around two different mean pres- 1090  
 sures:  $126 \pm 18 Pa$  and  $1444 \pm 471 Pa$ , in line with 1091  
 the two different values used for the particle den- 1092  
 sity throughout the CLPX series. Whatever the 1093  
 mass density, the mean pressure in axisymmetric 1094

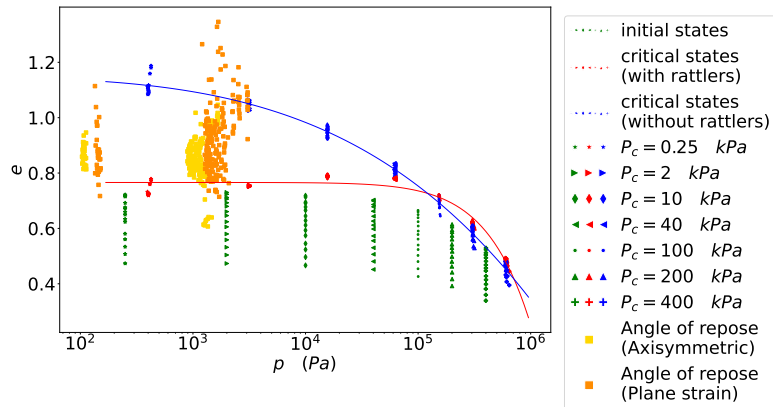


**Fig. 22:** Heaps' states after the collapse compared to the critical state line as determined in [28] from a large set of triaxial tests with different initial states in terms of void ratio and/or confining pressure  $P_c$

1095 heaps is lower than the mean pressure in plane  
 1096 strain heaps, and the dispersion in final void ratio  
 1097 is smaller. Most importantly, the heap states are  
 1098 clearly not consistent with the blue-colored (rat-  
 1099 tlers excluded) CSL serving as reference, which  
 1100 already suffices to exclude the assumption that a  
 1101 heap of particles under gravity is at critical state.

1102 For completeness, the angle of repose of these  
 1103 CLPX series is still furthermore directly compared  
 1104 in Figure 23 with the critical state friction angle  
 1105  $\phi_{crit}$  and the (porosity;mean stress)-dependent  
 1106 peak friction angle  $\phi_{peak}$  of the material, deter-  
 1107 mined on the triaxial simulations from [28]. The  
 1108 AOR is therein shown to be significantly differ-  
 1109 ent (higher from approx. 10 degrees) than  $\phi_{crit}$ .  
 1110 It actually lies in the observed interval for  $\phi_{peak}$ ,  
 1111 even though both are observed to be essentially  
 1112 different.

From the observations that the repose states  
 are not consistent with the shear strength proper-  
 ties of the granular material, neither the critical  
 one nor the maximum one, the AOR is concluded  
 to bear no constitutive nature. Interpreting the  
 repose stress state  $\sigma_{ij}^{glob}$  with its extreme principal  
 stresses  $\sigma_1^{glob} \geq \sigma_3^{glob}$  in terms of a mobilized fric-  
 tion angle  $\phi_{mob}$ , given in Equation 36 using the  
 soil mechanics sign convention:

$$\phi_{mob} = \arctan \left( \frac{\sigma_1^{glob} - \sigma_3^{glob}}{2\sqrt{\sigma_3^{glob}\sigma_1^{glob}}} \right) \quad (36)$$

1113 , no obvious correlation is actually found in  
 1114 Figure 24, no matter the shape model, between  
 1115 the mechanics of the heap,  $\phi_{mob}$ , and its geom-  
 1116 etry,  $\alpha$ , which would have been mandatory for a  
 1117 constitutive interpretation.

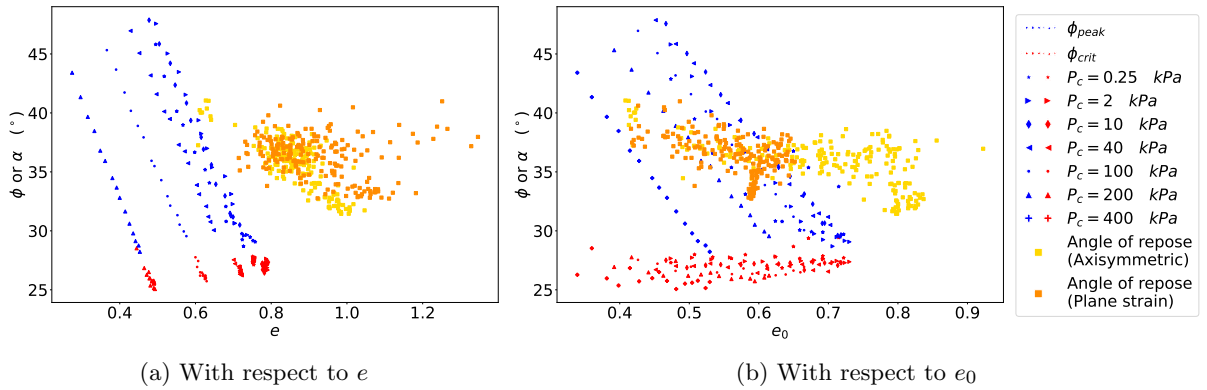


**Fig. 23:** Angle of repose  $\alpha$  and triaxial properties,  $\phi_{crit}$  and  $\phi_{peak}$ , with respect to void ratio (current,  $e$ , or initial,  $e_0$ )

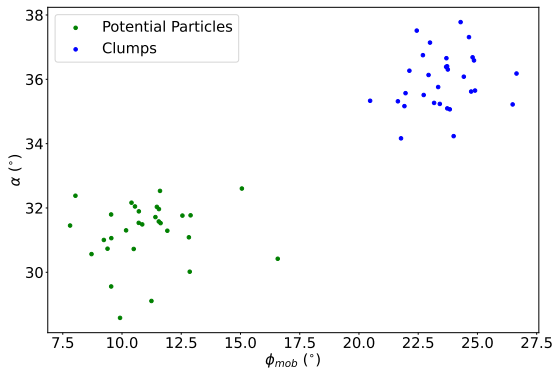


**Fig. 24:** Angle of repose  $\alpha$  against mobilized friction angle  $\phi_{mob}$  for heaps of the PP-CLP series.

#### 4.5 Effect of the sample size on the angle of repose

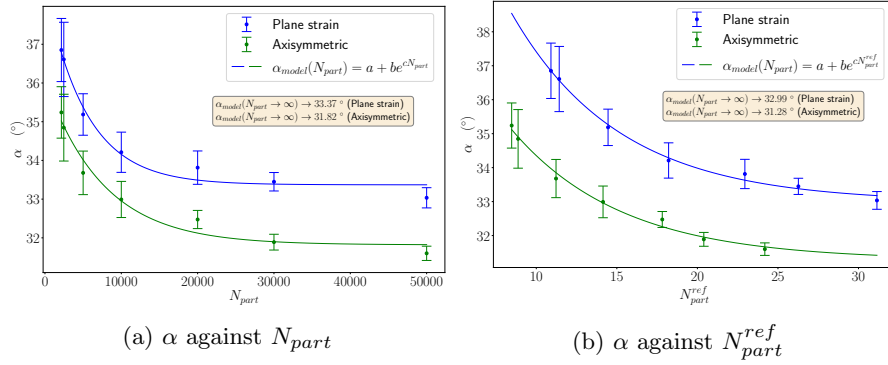
Since the default number of particles in both configurations is low compared e.g. to the number of particles necessary to constitute a REV for the triaxial tests with rigid boundaries (7500 in [28, 29] for the same or another granular material), it is finally investigated to which extent the sample size can affect the present discussion, performing a last “CLP5” series that adopts the clump model and an evolving number of particles  $N_{part}$  (see

Table 12 for all parameters). Doing so, the dimensions of the container are homothetically modified according to  $N_{part}^{1/3}$ , which insures to keep similar geometries (consistent length ratios between every 3 axes) when the total volume  $V \propto N_{part}$  increases.

Figure 25 shows the AOR values obtained in this CLP5 series, with error bars from the standard deviation computed on the ten simulations performed for each value of  $N_{part}$ . An exponential model is proposed to fit the data and provide an extrapolated value of  $\alpha$  for an infinite number of particles:

$$\alpha_{model}(N_{part}) = a + be^{cN_{part}} \quad (37)$$

with  $a$ ,  $b$  and  $c$  the three model parameters. Figure 25 (a) illustrates that the  $N_{part} = 2,150$  case is the only one where the AOR values from both configurations are compatible with the idea of a common value. On Figure 25 (b) the horizontal



**Fig. 25:** Effect of the sample size on the angle of repose - CLP5 series

1147 axis represents  $N_{part}^{ref}$ , the number of particle along  
 1148 one dimension of the base of the box:

$$N_{part}^{ref} = \left( \frac{N_{part}}{V_{box}} \right)^{\frac{1}{3}} L_{\eta} \quad (38)$$

1149 with  $V_{box} \in \{V_{cyl}, V_{par}\}$  and  $L_{\eta} \in \{R_{cyl}, L_{par}\}$ .

1150 For bigger systems with a higher  $N_{part}$  a  
 1151 clear difference appears, with a negligible stan-  
 1152 dard deviation. According to the exponential  
 1153 decay model, an asymptotic difference  
 1154 between the two configurations would be  $1.19^\circ$   
 1155 which corresponds to approximately 3.59% of the  
 1156 measurement in the plane strain configuration.

1157 The present dependency to  $N_{part}$  constitutes  
 1158 a last argument against the constitutive nature  
 1159 of the AOR, making fortuitous the near-similarity  
 1160 of  $\alpha$  initially observed between the two configura-  
 1161 tions, in connection with the particular values of  
 1162  $N_{part}$  used in the reference experiments.

## 5 Conclusion

1163

1164 In the framework of a round-robin activity provid-  
 1165 ing an experimental reference, the angle of repose  
 1166 of a granular material has been studied with  
 1167 DEM, adopting two distinct characterizations for  
 1168 particle shape: concave clumps of spheres and  
 1169 convex-simplified potential particles, with a quan-  
 1170 tification of the morphological differences between  
 1171 the two (and the experimental reference), in terms  
 1172 e.g. of convexity and sphericity.

1173 A methodological discussion has then been  
 1174 first proposed for generic angle of repose studies,  
 1175 designing systematic measurement procedures of  
 1176 the slope angle and of the void ratio of the heap,  
 1177 the latter being a possible factor of influence onto  
 1178 the former, as a fundamental property of granular  
 1179 matter.

1180 Physically, a thorough analysis provided a  
 1181 number of consistent observations that the AOR  
 1182 measured on the considered devices does not

1183 bear a constitutive nature but is instead process-  
 1184 dependent. In the comparison with experiments,  
 1185 while adopting a simpler measurement method  
 1186 of the AOR due to experimental limitations, the  
 1187 clump approach successfully predicted the AOR  
 1188 within a 8% tolerance. On the other hand, the  
 1189 potential particles underestimated to a greater  
 1190 extent the AOR, as expected due to their artificial  
 1191 convexity. Even though the material particles had  
 1192 a fairly high convexity value ( $C = 0.954$ ), neglect-  
 1193 ing their local concavities brought down the AOR  
 1194 from  $35.95 \pm 0.88^\circ$  to  $31.26 \pm 0.95^\circ$ .

1195 It is interesting to note that both the clump  
 1196 and the potential particle shape descriptions share  
 1197 the same dimensions in terms of a minimal bound-  
 1198 ing box and thus the same flatness and elongation  
 1199 values, prompting the need for a systematic inves-  
 1200 tigation of other particle-scale shape indices that  
 1201 would possibly affect the AOR.

## 1202 Appendix A YADE imple- 1203 mentations of 1204 visco-elasticity

1205 With reference to the normal contact law in  
 1206 Equation 2 and for the clump approach (which use  
 1207 here the `Ip2_ViscElMat_ViscElMat_ViscElPhys`  
 1208 and `Law2_ScGeom_ViscElPhys_Basic` YADE  
 1209 classes),  $c_n$  is computed from a given normal

1210 restitution coefficient  $e_n$  according to the mass-  
 1211 dependent expression of [30], recalled in Equation  
 1212 A1:

$$e_n = \begin{cases} \exp\left[-\frac{\beta}{\omega}\left(\pi - \arctan\frac{2\beta\omega}{\omega^2 - \beta^2}\right)\right] & \text{for } \beta < \frac{\omega_0}{\sqrt{2}} \\ \exp\left[-\frac{\beta}{\omega}\arctan\frac{2\beta\omega}{\omega^2 - \beta^2}\right] & \text{for } \beta \in \left[\frac{\omega_0}{\sqrt{2}}; \omega_0\right] \\ \exp\left[-\frac{\beta}{\Omega}\ln\frac{\beta + \Omega}{\beta - \Omega}\right] & \text{for } \beta > \omega_0 \end{cases} \quad (\text{A1})$$

1213 where  $\beta = \frac{c_n}{2m}$ ,  $\omega_0 = \sqrt{\frac{K_n}{m}}$ ,  $\omega = \sqrt{\omega_0^2 - \beta^2}$   
 1214 and  $\Omega = \sqrt{\beta^2 - \omega_0^2}$ , with  $m$  being the harmonic-  
 1215 average particle mass and  $K_n$  the normal contact  
 1216 stiffness. Equation A1 is solved inside YADE using  
 1217 a small number of Newton-Raphson iterations to  
 1218 make the inverse calculation of  $c_n$  based on the  
 1219 desired value of  $e_n$ . A straightforward calculation  
 1220 of  $c_n$  for the linear contact model has been pro-  
 1221 vided in Equation (B4) of [31] via curve-fitting of  
 1222 the exact solution of [30], which is not however  
 1223 employed here.

1224 For the potential particles approach (through,  
 1225 e.g., `Ip2_FrictMat_FrictMat_KnKsPhys` and  
 1226 `Law2_SCG_KnKsPhys_KnKsLaw` classes), a viscous  
 1227 damping parameter  $\beta_n$  serves as input for deriv-  
 1228 ing  $c_n$ , consistently with a desired  $e_n$  and [32] via  
 1229 Equation A2:

$$\beta_n = -\frac{\ln e_n}{\sqrt{\ln e_n^2 + \pi^2}} \quad (\text{A2})$$

1230 Then, the viscous damping coefficient is calcu-  
1231 lated as in Equation A3:

$$c_n = 2\beta\sqrt{m \cdot K_n} \quad (\text{A3})$$

## 1232 Appendix B A global stress 1233 tensor 1234 accounting for 1235 gravity

1236 In order to evaluate the stress state of the heap,  
1237 one has to compute the stress tensor from the con-  
1238 tact forces of all the contacts. Moreover, gravity  
1239 being present in the simulations and at the origin  
1240 of the movement, gravitational forces should thus  
1241 be accounted for. In this subsection:

- 1242 •  $\mathbb{S}$  is the set containing all particles,
- 1243 •  $\mathbb{C}^{ext}$  is the set containing all the contacts  
1244 between particles and boundaries,
- 1245 • the upper-script  $.^p$  specifies that the quantity is  
1246 taken for a particle  $p$ ,
- 1247 • the upper-script  $.^c$  specifies that the quantity is  
1248 taken for a contact  $c$ ,
- 1249 • the sub-script  $.,_{x_i}$  denotes the derivative with  
1250 respect to  $x_i$ ,
- 1251 • the total volume of the heap is noted  $V$  and can  
1252 be determined from the volumes of all tetrahe-  
1253 drons  $V^{tet}$  given by the Delaunay triangulation

on particles centers (see previous section 3.3.1): 1254

$$V = \bigcup_{p \in \mathbb{S}} V^{tet}, \quad 1255$$

- the number of underline denotes the order of a 1256  
tensor ( $\underline{\cdot}$  for vectors and  $\underline{\underline{\cdot}}$  for matrices), 1257
- the Kronecker symbol  $\delta_{ij}$  and Einstein's nota- 1258  
tion will be used, 1259
- classical sign convention for stress is adopted, 1260  
where the traction vector  $\underline{t} = \underline{\underline{\sigma}} \cdot \underline{n}$  applies onto 1261  
the system for an outwards normal  $\underline{n}$ . 1262

The global stress tensor  $\underline{\underline{\sigma}}^{glob}$  can be expressed 1263  
according to the local stress tensor  $\underline{\underline{\sigma}}$ : 1264

$$\underline{\underline{\sigma}}^{glob} = \frac{1}{V} \int_V \underline{\underline{\sigma}} dV \quad (\text{B4})$$

One can compute  $\underline{\underline{\sigma}}$  using the divergence of the 1265  
third order tensor  $\underline{\underline{\sigma}} \otimes \underline{x}$  (with  $\underline{x}$  the position of any 1266  
point in  $V$  with respect to a given, even though 1267  
arbitrary, origin): 1268

$$(\sigma_{ik}x_j)_{,k} = \sigma_{ik,k}x_j + \sigma_{ik}x_{j,k} \quad (\text{B5})$$

Since the measurement is made when the heap 1269  
is under equilibrium, the following equation holds, 1270  
denoting  $\underline{g}$  the gravitational acceleration and  $\rho$  the 1271  
particle density: 1272

$$\sigma_{ij,j} = -\rho g_i \quad (\text{B6})$$

Moreover,  $x_{j,k} = \delta_{jk}$ , thus: 1273

$$\sigma_{ik}x_{j,k} = \sigma_{ij} \quad (\text{B7})$$

1274 By replacing Equation B6 and Equation B7 in  
1275 Equation B5 one gets:

$$\sigma_{ij} = (\sigma_{ik}x_j)_{,k} + \rho g_i x_j \quad (\text{B8})$$

Equation B4 then gives:

$$\sigma_{ij}^{glob} = \frac{1}{V} \int_V \left( (\sigma_{ik}x_j)_{,k} + \rho g_i x_j \right) dV \quad (\text{B9})$$

$$= \frac{1}{V} \sum_{p \in \mathbb{S}} \int_{V^p} \left( (\sigma_{ik}x_j)_{,k} + \rho g_i x_j \right) dV \quad (\text{B10})$$

because  $\sigma_{ij} \neq 0$  only on  $V^p$

$$= \underbrace{\frac{1}{V} \sum_{p \in \mathbb{S}} \int_{V^p} (\sigma_{ik}x_j)_{,k} dV}_{\sigma_{ij}^C} + \underbrace{\frac{1}{V} \sum_{p \in \mathbb{S}} \int_{V^p} \rho g_i x_j dV}_{\sigma_{ij}^G} \quad (\text{B11})$$

1276 Particles having an homogeneous density, one  
1277 furthermore has, with  $m^p$  and  $\underline{x}^p$  the mass and  
1278 center of  $p$  :

$$\int_{V^p} \rho x_j dV = m^p x_j^p \quad (\text{B12})$$

1279 The part of  $\underline{\underline{\sigma}}$  due to gravity ( $\sigma_{ij}^G$ ) can thus be  
1280 written:

$$\sigma_{ij}^G = \frac{1}{V} \sum_{p \in \mathbb{S}} m^p g_i x_j^p \quad (\text{B13})$$

1281 As for the part due to contacts ( $\sigma_{ij}^C$ ), Green-  
1282 Ostrogradski theorem gives:

$$\sigma_{ij}^C = \frac{1}{V} \sum_{p \in \mathbb{S}} \int_{\partial V^p} \sigma_{ik} x_j n_k dS \quad (\text{B14})$$

Considering the traction vector  $\underline{t} = \underline{\underline{\sigma}} \cdot \underline{n}$ , one  
has:

$$\sigma_{ij}^C = \frac{1}{V} \sum_{p \in \mathbb{S}} \int_{\partial V^p} t_i x_j dS \quad (\text{B15})$$

The traction vector is not nil only on contact  
points. Since the system is closed, contact forces  
between particles cancel each other leaving only  
forces coming from outside of  $V$ . As a conse-  
quence, one can only consider the contact forces  
between particles and walls. For these contacts  $f^c$   
denotes the contact force exerted by the wall on  
the particle and  $x^c$  the contact point. One has:

$$\sigma_{ij}^C = \frac{1}{V} \sum_{c \in \mathbb{C}^{ext}} f_i^c x_j^c \quad (\text{B16})$$

Finally, the global stress tensor for a stable  
heap of particles made of homogeneous particles  
and subjected to gravity is:

$$\sigma_{ij}^{glob} = \frac{1}{V} \sum_{c \in \mathbb{C}^{ext}} f_i^c x_j^c + \frac{1}{V} \sum_{p \in V} m^p g_i x_j^p \quad (\text{B17})$$

The mean stress can then be computed as  $p =$   
 $\frac{\text{Tr}(\underline{\underline{\sigma}}^{glob})}{3}$ .

## Appendix C Influence of the wall velocity

In both configurations a wall holding the particles  
moves in order to let them fall. The way parti-  
cles fall depends on the velocity at which the wall

1303 moves, but once the heap is stabilized the mea-  
 1304 surement of the AOR could be the same no matter  
 1305 the velocity. This could allow the increase of the  
 1306 wall velocity  $V_{wall}$  and thus the decrease of the  
 1307 time cost. To know the influence of  $V_{wall}$  on the  
 1308 AOR, a series of simulations, CLP3, is performed  
 1309 with the clump model. Its parameters are given in  
 1310 Table C1. For each value of the speed-up factor,  
 1311 10 simulations are performed.

1312 Figure C1 shows the results of the CLP3 series.  
 1313 The symbols correspond to the mean measure-  
 1314 ment over the 10 simulations performed with the  
 1315 same  $V_{wall}$  and the error bars represent the stan-  
 1316 dard deviation. One can state that in the plane  
 1317 strain configuration  $V_{wall}$  does not have an effect  
 1318 on  $\alpha$ . However, in the axisymmetric configura-  
 1319 tion,  $\alpha$  decreases sharply in the transition zone  
 1320  $10 < V_{wall}/V_{wall}^{ref} < 100$ . In the plane strain con-  
 1321 figuration,  $V_{wall}/V_{wall}^{ref} = 10,000$  can thus be used,  
 1322 while one should restrict to  $V_{wall}/V_{wall}^{ref} = 10$  in  
 1323 the axisymmetric configuration. Table C2 gives a  
 1324 summary of the value of  $V_{wall}$  used throughout all  
 1325 AOR simulations in this paper.

## 1326 Data availability

1327 All YADE scripts used to perform the PP-CLP  
 1328 series are available online at [https://forgemia.  
 1329 inra.fr/sacha.duverger/aor\\_nc\\_aix](https://forgemia.inra.fr/sacha.duverger/aor_nc_aix).

## Acknowledgements 1330

We thank the Japanese Geotechnical Society for  
 1331 organizing the DEM round robin test that moti-  
 1332 vated this study. The efforts of Dr Shuji Moriguchi  
 1333 (Tohoku University) are in particular gratefully  
 1334 acknowledged. We also acknowledge the support  
 1335 from the French "Sud" region to the recent LS-  
 1336 ENROC project with an acquisition of a server  
 1337 machine that could accomodate the 980 simula-  
 1338 tions presented herein. 1339

## Compliance with Ethical 1340

### Standards 1341

The authors have no competing interests to  
 1342 declare that are relevant to the content of this  
 1343 article. 1344

## References 1345

- 1346 [1] Derek Geldart, EC Abdullah, A Hassanpour,  
 1347 LC Nwoke, and IJCP Wouters. Character-  
 1348 ization of powder flowability using measure-  
 1349 ment of angle of repose. *China Particuology*,  
 1350 4(3-4):104–107, 2006.
- 1351 [2] Hamzah M Beakawi Al-Hashemi and Omar  
 1352 S Baghabra Al-Amoudi. A review on the  
 1353 angle of repose of granular materials. *Powder  
 1354 technology*, 330:397–417, 2018.
- 1355 [3] Pascale C Rousé. Comparison of methods  
 1356 for the measurement of the angle of repose

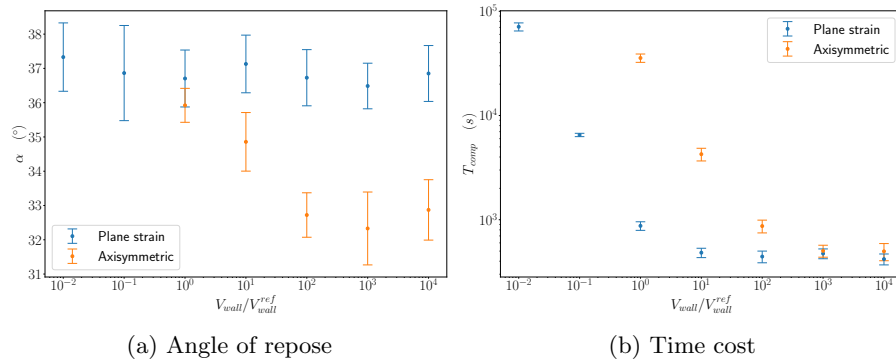


**Fig. C1:** Wall velocity influence on the angle of repose and on the time cost - CLP3

- of granular materials. *Geotechnical Testing Journal*, 37(1):164–168, 2014.
- [4] Yukio Nakata, Shuji Moriguchi, Shintaro Kajiyama, Ryunosuke Kido, Naotaka Kikkawa, Hidetaka Saomoto, Daiki Takano, and Yosuke Higo. Experimental data of 3d printed granular material for verification of discrete element modeling simulation. *Soils and Foundations*, 62(4):101178, 2022.
- [5] M. D. Bolton. The strength and dilatancy of sands. *Géotechnique*, 36(1):65–78, 1986.
- [6] Michael Rackl and Kevin J. Hanley. A methodical calibration procedure for discrete element models. *Powder Technology*, 307:73–83, 2017.
- [7] Thomas Roessler, Christian Richter, André Katterfeld, and Frank Will. Development of a standard calibration procedure for the dem parameters of cohesionless bulk materials – part i: Solving the problem of ambiguous parameter combinations. *Powder Technology*, 343:803 – 812, 2019.
- [8] H.G. Matuttis, S. Luding, and H.J. Herrmann. Discrete element simulations of dense packings and heaps made of spherical and non-spherical particles. *Powder Technology*, 109(1):278–292, 2000.
- [9] YC Zhou, BH Xu, AB Yu, and Paul Zulli. Numerical investigation of the angle of repose of monosized spheres. *Physical Review E*, 64(2):021301, 2001.
- [10] Miki Y Matsuo, Daisuke Nishiura, and Hide Sakaguchi. Geometric effect of angle of repose revisited. *Granular Matter*, 16(4):441–447, 2014.
- [11] Thorsten Pöschel and Volkhard Buchholtz. Static friction phenomena in granular materials: Coulomb law versus particle geometry. *Phys. Rev. Lett.*, 71:3963–3966, 1993.
- [12] Hao Chen, Shiwei Zhao, and Xiaowen Zhou. Dem investigation of angle of repose for super-ellipsoidal particles. *Particuology*, 50:53–66, 2020.
- [13] Nikola Topić, Jason AC Gallas, and Thorsten

- 1401 Pöschel. Nonuniformities in the angle  
1402 of repose and packing fraction of large  
1403 heaps of particles. *Physical review letters*,  
1404 109(12):128001, 2012.
- 1405 [14] Fathan Akbar, Elfi Yuliza, Nadya Amalia,  
1406 Handika Dany Rahmayanti, and Mikrajuddin  
1407 Abdullah. The slope of dry granular materials  
1408 surface is generally curved. *Granular Matter*,  
1409 24(69), 2022.
- 1410 [15] Hidetaka Saomoto, Naotaka Kikkawa, Shuji  
1411 Moriguchi, Yukio Nakata, Masahide Otsubo,  
1412 Vasileios Angelidakis, Yi Pik Cheng, Kevin  
1413 Chew, Gabriele Chiaro, Jérôme Duriez,  
1414 Sacha Duverger, Joaquín Irazábal González,  
1415 Mingjing Jiang, Yohei Karasaki, Akiko Kono,  
1416 Xintong Li, Zhuyuan Lin, Asen Liu, Sadegh  
1417 Nadimi, Hitoshi Nakase, Daisuke Nishiura,  
1418 Utsa Rashique, Hiroyuki Shimizu, Kumpei  
1419 Tsuji, Takashi Watanabe, Xiaomin Xu, and  
1420 Mourad Zeghal. Round robin test on angle  
1421 of repose: Dem simulation results collected  
1422 from 16 groups around the world. *Soils and*  
1423 *Foundations*, 63(1):101272, 2023.
- 1424 [16] V. Smilauer et al. *Yade Documentation 3rd*  
1425 *ed.* The Yade Project, 2021. [http://yade-](http://yade-dem.org/doc/)  
1426 [dem.org/doc/](http://yade-dem.org/doc/).
- 1427 [17] Vasileios Angelidakis, Sadegh Nadimi,  
1428 Masahide Otsubo, and Stefano Utili.  
1429 CLUMP: A Code Library to generate Uni-  
1430 versal Multi-sphere Particles. *SoftwareX*,  
1431 15:100735, 2021.
- [18] Jean-Francois Ferrellec and Glenn R McDow- 1432  
ell. A method to model realistic particle 1433  
shape and inertia in DEM. *Granular Matter*, 1434  
12(5):459–467, 2010. 1435
- [19] Guy Tinmouth Houlsby. Potential particles: 1436  
a method for modelling non-circular parti- 1437  
cles in DEM. *Computers and Geotechnics*, 1438  
36(6):953 – 959, 2009. 1439
- [20] Chia Weng Boon, Guy Tinmouth Houlsby, 1440  
and Stefano Utili. A new contact detec- 1441  
tion algorithm for three-dimensional non- 1442  
spherical particles. *Powder Technology*, 1443  
248:94 – 102, 2013. Discrete Element Mod- 1444  
elling. 1445
- [21] Reid Kawamoto, Edward Andò, Gioacchino 1446  
Viggiani, and José E Andrade. Level set dis- 1447  
crete element method for three-dimensional 1448  
computations with triaxial case study. *Jour- 1449  
nal of the Mechanics and Physics of Solids*, 1450  
91:1–13, 2016. 1451
- [22] Jérôme Duriez and Cédric Galusinski. A 1452  
level set-discrete element method in yade 1453  
for numerical, micro-scale, geomechanics with 1454  
refined grain shapes. *Computers & Geo- 1455  
sciences*, 157:104936, 2021. 1456
- [23] Jérôme Duriez and Stéphane Bonelli. Pre- 1457  
cision and computational costs of Level Set- 1458  
Discrete Element Method (LS-DEM) with 1459  
respect to DEM. *Computers and Geotechnics*, 1460  
134:104033, 2021. 1461

- 1462 [24] Vasileios Angelidakis, Sadegh Nadimi, and  
1463 Stefano Utili. SHape Analyser for Particle  
1464 Engineering (SHAPE): Seamless characteri-  
1465 sation and simplification of particle morphol-  
1466 ogy from imaging data. *Computer Physics  
1467 Communications*, 265:107983, 2021.
- 1468 [25] Hakon Wadell. Volume, shape, and round-  
1469 ness of rock particles. *The Journal of Geology*,  
1470 40(5):443–451, 1932.
- 1471 [26] Bruno Chareyre and Pascal Villard. Dynamic  
1472 spar elements and discrete element methods  
1473 in two dimensions for the modeling of soil-  
1474 inclusion problems. *Journal of Engineering  
1475 Mechanics*, 131(7):689–698, 2005.
- 1476 [27] Claudio Rocchini and Paolo Cignoni. Gener-  
1477 ating random points in a tetrahedron. *Jour-  
1478 nal of graphics Tools*, 5(4):9–12, 2000.
- 1479 [28] Sacha Duverger, Jérôme Duriez, Pierre  
1480 Philippe, and Stéphane Bonelli. Rattlers’  
1481 involvement for possibly looser critical states  
1482 under higher mean stress. In *EPJ Web of  
1483 Conferences*, volume 249, page 11002. EDP  
1484 Sciences, 2021.
- 1485 [29] T. Mohamed, J. Duriez, G. Veylon, and  
1486 L. Peyras. DEM models using direct and  
1487 indirect shape descriptions for Toyoura sand  
1488 along monotonous loading paths. *Computers  
1489 and Geotechnics*, 142:104551, 2022.
- 1490 [30] Thomas Schwager and Thorsten Pöschel.  
1491 Coefficient of restitution and linear-dashpot  
model revisited. *Granular Matter*, 9(6):465–  
469, 2007.
- [31] Colin Thornton, Sharen J Cummins, and  
Paul W Cleary. An investigation of the  
comparative behaviour of alternative con-  
tact force models during inelastic collisions.  
*Powder technology*, 233:30–46, 2013.
- [32] D Antypov and JA Elliott. On an analytical  
solution for the damped hertzian spring. *EPL  
(Europhysics Letters)*, 94(5):50004, 2011.

**Table 11:** Parameters used when investigating a possible influence of  $e_0$  (CLP4 series, 200 simulations in total)

Configuration	$N_{part}$	$\rho$	$e_0$	Number of samples for each $e_0$
Plane strain	2, 150	10,000 $kg/m^3$	$0.414 \pm 0.010$	10
			$0.459 \pm 0.009$	
			$0.480 \pm 0.008$	
			$0.495 \pm 0.006$	
			$0.504 \pm 0.008$	
			$0.528 \pm 0.006$	
			$0.536 \pm 0.008$	
			$0.553 \pm 0.010$	
			$0.567 \pm 0.012$	
			$0.574 \pm 0.007$	
Axisymmetric	2, 468	10,000 $kg/m^3$	$0.419 \pm 0.006$	10
			$0.486 \pm 0.006$	
			$0.525 \pm 0.009$	
			$0.553 \pm 0.006$	
			$0.577 \pm 0.011$	
			$0.607 \pm 0.018$	
			$0.626 \pm 0.014$	
			$0.632 \pm 0.010$	
$0.655 \pm 0.012$				
$0.671 \pm 0.016$				

Configuration	$N_{part}$	$\rho$	$e_0$	Number of samples
Plane strain	2, 150 2, 468 5,000 10,000 20,000 30,000 50,000	10,000 $kg/m^3$	$0.603 \pm 0.010$	10
			$0.604 \pm 0.009$	
			$0.596 \pm 0.005$	
			$0.596 \pm 0.003$	
			$0.594 \pm 0.002$	
			$0.591 \pm 0.003$	
			$0.588 \pm 0.001$	
			$0.705 \pm 0.011$	
Axisymmetric			$0.693 \pm 0.010$	
			$0.729 \pm 0.017$	
			$0.741 \pm 0.006$	
			$0.758 \pm 0.008$	
			$0.746 \pm 0.016$	
			$0.736 \pm 0.004$	

**Table 12:** Parameters of heap simulations investigating the influence of  $N_{part}$  (CLP5 series, 140 simulations in total)

Configuration	$N_{part}$	$\rho$	$V_{wall}/V^{ref}$	$e_0$	Number of samples
Plane strain	2,150	10,000 kg/m <sup>3</sup>	$10^i$ for $i \in [-2, 4] \cap \mathbf{N}$	$0.603 \pm 0.010$	10
Axisymmetric	2,468		$10^i$ for $i \in [0, 4] \cap \mathbf{N}$	$0.693 \pm 0.010$	

**Table C1:** Parameters of heap simulations investigating  $V_{wall}$  influence (CLP3 series, 120 simulations in total)

Series	CLP1	CLP2	CLP4	CLP5	PP1	PP-CLP
$V_{cyl}/V_{cyl}^{ref}$	1	1	10	10	-	-
$V_{par}/V_{par}^{ref}$	1	1	$10^4$	$10^4$	$10^3$	$10^3$

**Table C2:** Wall velocity for all series of simulations